PHYSICAL REVIEW D **79,** 023517 (2009)

Complete treatment of galaxy two-point statistics: Gravitational lensing effects and redshift-space distortions

Jaiyul Yoo*

Harvard-Smithsonian Center for Astrophysics, Harvard University, 60 Garden Street, Cambridge, Massachusetts 02138, USA

(Received 22 August 2008; published 22 January 2009)

We present a coherent theoretical framework for computing gravitational lensing effects and redshift-space distortions in an inhomogeneous universe and investigate their impacts on galaxy two-point statistics. Adopting the linearized Friedmann-Lemaître-Robertson-Walker metric, we derive the gravitational lensing and the generalized Sachs-Wolfe effects that include the weak lensing distortion, magnification, and time delay effects, and the redshift-space distortion, Sachs-Wolfe, and integrated Sachs-Wolfe effects, respectively. Based on this framework, we first compute their effects on observed source fluctuations, separating them as two physically distinct origins: the volume effect that involves the change of volume and is always present in galaxy two-point statistics, and the source effect that depends on the intrinsic properties of source populations. Then we identify several terms that are ignored in the standard method, and we compute the observed galaxy two-point statistics, an ensemble average of all the combinations of the intrinsic source fluctuations and the additional contributions from the gravitational lensing and the generalized Sachs-Wolfe effects. This unified treatment of galaxy two-point statistics clarifies the relation of the gravitational lensing and the generalized Sachs-Wolfe effects to the metric perturbations and the underlying matter fluctuations. For near-future dark energy surveys, we compute additional contributions to the observed galaxy two-point statistics and analyze their impact on the anisotropic structure. Thorough theoretical modeling of galaxy two-point statistics would be not only necessary to analyze precision measurements from upcoming dark energy surveys, but also provide further discriminatory power in understanding the underlying physical mechanisms.

DOI: 10.1103/PhysRevD.79.023517 PACS numbers: 98.80.−k, 98.62.Py, 98.65.−r, 98.80.Jk

I. INTRODUCTION

The standard inflationary models with a single inflaton potential predict a nearly perfect Gaussian spectrum of primordial fluctuations [1–5]. Two-point statistics, correlation function in real space and power spectrum in Fourier space, constitutes a complete description of Gaussian random fields, and it has been widely used to understand the physics of the early Universe from measurements of the cosmic microwave background and large-scale structure. The recent discovery [6,7] of the late time acceleration of the Universe has spurred extensive investigations of a mysterious energy component with negative pressure, dubbed dark energy. Observationally, upcoming dark energy surveys will measure galaxy two-point statistics with unprecedented precision from millions of galaxies, constraining the expansion history and the spatial curvature of the Universe. Consequently, accurate theoretical modeling of galaxy two-point statistics would be crucial to take full advantage of the promise that these future surveys will deliver.

In achieving this goal, complications arise notably from the nonlinear evolution of matter and scale dependence of galaxy bias. In this paper, we limit ourselves to the linear bias model [8] and study the linear theory predictions and its corrections, considering that recent attention has been paid to measuring galaxy two-point statistics in the linear regime (e.g., [9–12]). However, measurement precision is often highest on nonlinear scales, and proper modeling of galaxy bias on nonlinear scales can substantially increase the leverage to constrain the underlying physics (see, e.g., [13–19]).

Further complication arises from the distortion of redshift-space structure by peculiar velocities, which results in anisotropy from otherwise isotropic two-point statistics [20,21]. The standard practice is to analyze the angle-averaged correlation function or power spectrum, or to construct a linear combination of their multipole components, suppressing the angular dependence of two-point statistics. However, analyzing the full anisotropic structure, though observationally challenging, can utilize additional information that is lost to some degree in the standard practice [22–25].

Gravitational lensing, often assumed to be negligible in galaxy two-point statistics, deflects the propagation of light rays, displacing the position of observed galaxies, and it alters the unit area on the sky and magnifies the observed flux, changing the observed number density of galaxies. The former effect on two-point statistics is to convolve it with the power spectrum of the lensing potential, smoothing out the features in galaxy two-point statistics [26]. The latter effect, known as the magnification bias [27], is often used to measure the galaxy-matter cross correlation function from two source populations separated by large line-

*jyoo@cfa.harvard.edu

of-sight distance [28,29]. Recent work [30–32] showed that these effects on galaxy two-point statistics are non-negligible at the level of accuracy adequate for upcoming dark energy surveys.

However, it is unclear whether this list of additional contributions on galaxy two-point statistics is exhaustive, and what are the contribution terms that are ignored in the standard method but need to be considered if higher accuracy is dictated by observations. Here we present a coherent theoretical framework for computing gravitational lensing effects and redshift-space distortions, and investigate their impacts on galaxy two-point statistics in an inhomogeneous universe. Our treatment generalizes the early work [30] and complements the recent work [31,32], providing a unified description of galaxy two-point statistics. However, we emphasize that these effects naturally arise from metric perturbations in our approach, comprising a complete and exhaustive set of additional (linear order) contributions to galaxy two-point statistics.

The rest of this paper is organized as follows. In Sec. II, we describe our notation for the Friedmann-Lemaître-Robertson-Walker (FLRW) metric and derive the gravitational lensing and the generalized Sachs-Wolfe effects. In Sec. III, we study their impacts on source galaxy fluctuations and discuss their correspondence to the standard redshift-space distortion and gravitational lensing effect. In Sec. IV A, we derive the observed galaxy two-point statistics in real space and in Fourier space, and we compare the effects of each contribution term on the observed galaxy two-point statistics in Sec. IV B. We conclude in Sec. V with a discussion of the further improvement of our approach.

II. FORMALISM

Here we describe our notation for a background metric in an inhomogeneous universe and derive governing equations for nonrelativistic matter in Sec. II A. Combining these with photon geodesic equations, we derive the generalized Sachs-Wolfe (Sec. II B) and the gravitational lensing (Sec. II C) effects, developing a coherent framework for describing how matter fluctuations affect observable quantities.

A. Metric and perturbations

We assume that the homogeneous and isotropic background of the Universe is described by the FLRW metric and its inhomogeneous part is represented by the perturbations for the cosmological fluids and the spacetime geometry:

$$ds^2 = -a^2(\eta)[1+2\psi]d\eta^2 + a^2(\eta)[1+2\phi]g^{(3)}_{\alpha\beta}dx^\alpha dx^\beta, \tag{1}$$

with the metric tensor for a three space of constant spatial curvature $K = -H_0^2(1-\Omega_0)$,

$$g^{(3)}_{\alpha\beta}dx^\alpha dx^\beta = d\chi^2 + r^2(\chi)d\Omega^2, \tag{2}$$

where $a(\eta)$ is the scale factor for the expansion of the background as a function of the conformal time η, and the comoving angular diameter distance is $r(\chi) = K^{-1/2}\sin(\sqrt{K}\chi)$ for a closed universe $K>0$ and $(-K)^{-1/2}\sinh(\sqrt{-K}\chi)$ for an open universe $K<0$, where χ is the comoving line-of-sight distance. The flat limit can be obtained as $K\to 0$. We will denote the covariant derivative of a three tensor with respect to $g^{(3)}_{\alpha\beta}$ as a vertical bar and the covariant derivative in the spacetime metric as a semicolon in the following. Here Latin indices represent 4D spacetime components, and Greek indices run from 1 to 3, representing the spatial part of the metric. Throughout the paper, we set the speed of light $c\equiv 1$.

We express the perturbations in the conformal Newtonian gauge, where ψ and ϕ correspond to the intuitive physical quantities, i.e., Newtonian potential and Newtonian curvature. This choice of gauge condition leaves no residual degree of freedom up to the first order in perturbations. Here we only consider scalar perturbations, as primordial vector perturbations decay quickly in a universe with ordinary components and the current upper limit on tensor perturbations is order of magnitude smaller than the amplitude of scalar perturbations (e.g., [33–35]).

Given the stress energy tensor T^{ab} of cosmological components, the evolution of the matter and metric perturbations is governed by the Einstein equations $G_{ab} = 8\pi G T_{ab}$, and the Bianchi identities $T^{ab}{}_{;b} = 0$ guarantee the conservation of energy and momentum (e.g., [5,36–39]). Current cosmological observations favor a universe dominated by dark energy, but with nonrelativistic matter as the major source of metric perturbations. In this universe, the scalar Einstein equations are

$$(k^2 - 3K)\phi = \frac{3H_0^2}{2}\Omega_m\left[\frac{\delta}{a} + 3H\frac{v}{k}\right], \tag{3}$$

$$\psi = -\phi, \tag{4}$$

where δ is the density perturbation in nonrelativistic matter. The Hubble parameter is $H = \dot{a}/a$, where the overdot is the derivative with respect to time, $dt = a d\eta$. The matter density and the Hubble parameters at the present day a_0 are denoted as Ω_m and H_0, respectively. The Newtonian curvature is identical to the Newtonian potential with the opposite sign ($\psi = -\phi$) in the matter-dominated era, where there is vanishing anisotropic stress. The conservation of energy momentum provides the continuity and Euler equations,

$$\dot{\delta} + \frac{k}{a}v = -3\dot{\phi}, \tag{5}$$

$$\dot{v} + Hv = \frac{k}{a}\psi, \tag{6}$$

where v is the velocity of nonrelativistic matter in units of c. In the conformal Newtonian gauge, the relativistic equations on subhorizon scales correspond to the usual Newtonian equations,

$$\nabla^2\psi = \frac{3H_0^2}{2}\Omega_m\frac{\delta}{a}, \tag{7}$$

$$\mathbf{v} = -\frac{2}{3}\frac{a^2Hf}{\Omega_m H_0^2}\nabla\psi, \tag{8}$$

where $f = d\ln D/d\ln a$ and D is a growth factor of the matter density perturbation. The evolution of the density perturbation is related to the Newtonian potential by

$$\ddot{\delta} + 2H\dot{\delta} = \nabla^2\psi, \tag{9}$$

and the growth factor D is a growing solution of this differential equation, normalized to a unity at a_0. Full relativistic consideration results in additional multiple terms in the right-hand side of the equation (e.g., [5]), but they are suppressed at least by the ratio of a characteristic scale $1/k$ to the Hubble distance $1/H$. Note that we have interchangeably expressed equations in Fourier space and configuration space, which is valid to the linear order in perturbations and significantly simplifies the manipulations.

B. Geodesic equations and Sachs-Wolfe effects

The propagation of light rays is described by a photon geodesic $x^a(\lambda)$ with an affine parameter λ, and a null vector $k^a = dx^a/d\lambda$ tangent to x^a is determined by the null equation ($ds^2 = k^a k_a = 0$) and the geodesic equations ($k^a{}_{;b}k^b = 0$). In a perturbed FLRW universe, the null vector can be expressed as

$$k^0 = \frac{\nu}{a}(1+\delta\nu), \qquad k^\alpha = -\frac{\nu}{a}(e^\alpha + \delta e^\alpha), \tag{10}$$

where ν and e^α are the photon frequency and its (time-reversed) propagation direction from the observer, and the dimensionless quantities $\delta\nu$ and δe^α represent their perturbations. In a homogeneous expanding universe, the null vector follows the usual relations $\nu \propto 1/a$, $e^\alpha e_\alpha = 1$, and $de^\alpha/d\eta = e^\beta e^\alpha_{|\beta}$, and indeed Eq. (10) may be derived from the null and the geodesic equations. For a comoving observer whose rest frame has vanishing energy flux, the four velocity is $u^a = (1/a, 0)$ and the observed frequency $\nu_{\rm obs}$ of a photon source is related to the frequency ν_e at the emission by a redshift parameter,

$$1+z = \frac{(k^a u_a)_e}{(k^a u_a)_{\rm obs}} = \frac{\nu_e}{\nu_{\rm obs}} = \frac{1}{a_e}, \tag{11}$$

where we assumed $a_{\rm obs} = a_0 = 1$.

In an inhomogeneous universe, the observed redshift $z_{\rm obs}$ deviates from the true redshift z. The perturbation in the null equation is

$$e^\alpha\delta e_\alpha = \delta\nu + \psi - \phi, \tag{12}$$

and perturbations in the geodesic equations for the temporal and spatial components are

$$\frac{d}{dy}(\delta\nu + \psi) = \psi_{,\alpha}e^\alpha - \frac{d\phi}{d\eta}, \tag{13}$$

$$\frac{d}{dy}(\delta e^\alpha + 2\phi e^\alpha) = \delta e^\beta e^\alpha_{|\beta} - \delta\nu\frac{de^\alpha}{d\eta} + \psi^{|\alpha} - \phi^{|\alpha}, \tag{14}$$

where we used the zeroth order null geodesic $d/dy \equiv \partial_\eta - e^\alpha\partial_\alpha = (a/\nu)(d/d\lambda)$ and kept the terms to the first order in perturbations.

The four velocity of a comoving observer is now $u^a = ((1-\psi)/a, v^\alpha/a)$ and the observed redshift is

$$1+z_{\rm obs} = \frac{(k^a u_a)_e}{(k^a u_a)_{\rm obs}} = (1+z)[1 + (\delta\nu + \psi + v_\alpha e^\alpha)^e_o]. \tag{15}$$

This can be further simplified by using Eq. (13) as

$$1+z_{\rm obs} = (1+z)\times\Big[1 + V(z) - V(0) - \psi(z) + \psi(0) + \int_0^y dy\frac{\partial}{\partial\eta}(\phi-\psi)\Big], \tag{16}$$

where $V = v_\alpha e^\alpha$ is the line-of-sight velocity [30,40,41]. The additional terms in the square bracket alter the simple redshift-distance relation in Eq. (11), giving rise to the standard redshift-space distortion by peculiar velocities, the Sachs-Wolfe effect by gravitational redshift, and the integrated Sachs-Wolfe effect by the time evolution of gravitational potential across which photons propagate. Hereafter we will collectively refer to these effects as the generalized Sachs-Wolfe effect.

C. Gravitational lensing

In a homogeneous universe, the gravitational lensing effects vanish and light rays propagate with the direction unchanged. For a photon source at $\hat{\mathbf{z}}$-axis in an inhomogeneous universe, the propagation direction from the observer is $\hat{\mathbf{n}} = e^\alpha = (0,0,1)$ and the null vector is $k^{x,y} = -(\nu/a)\delta e^{x,y}$. The null vector is further related to the photon position $r(\chi)\hat{\mathbf{n}} = (x,y)$ on the sky at any time by

$$k^{x,y} = \frac{d}{d\lambda}(r\hat{\mathbf{n}}) = \frac{\nu}{a}\frac{d}{dy}(r\hat{\mathbf{n}}), \tag{17}$$

where we replace the derivative with respect to the affine parameter by using the zeroth order null geodesic, consistent to the first order in perturbations. The spatial component of the geodesic equation [Eq. (14)] is then

$$\frac{d}{dy}(\delta e^{x,y}) = -\frac{d^2}{dy^2}(r\hat{\mathbf{n}}) = \psi^{|\alpha} - \phi^{|\alpha} = 2\psi^{|\alpha}. \quad (18)$$

Since gravitational lensing conserves the surface brightness, the observed surface brightness $I_{\rm obs}(\hat{\mathbf{n}})$ on the sky is simply the intrinsic surface brightness at the source position $\hat{\mathbf{s}}$: $I_{\rm obs}(\hat{\mathbf{n}}) = I(\hat{\mathbf{s}})$, and the source position $\hat{\mathbf{s}}$ can be obtained by integrating Eq. (18) along the photon geodesic

$$\hat{\mathbf{s}} = \hat{\mathbf{n}} + \hat{\nabla}\Psi(\hat{\mathbf{n}}), \quad (19)$$

with the projected lensing potential

$$\Psi(\hat{\mathbf{n}}) = -2\int_0^{y_s} dy' \int_0^{y'} dy \frac{\psi(y)}{r(\chi_s)r(\chi)} = -2\int_0^{y_s} dy\,\psi(y)\frac{r(\chi_s-\chi)}{r(\chi_s)r(\chi)}, \quad (20)$$

where $\hat{\nabla}$ is the derivative with respect to $\hat{\mathbf{n}}$, and $\chi_s = \int_0^{z_s} dz/H(z)$ is the comoving line-of-sight distance to the source redshift z_s. The integration along the unperturbed photon geodesic dy is often called the Born approximation. Following the literature, we take the geodesic as the photon radial direction $d\chi$, but note that $d/d\chi = \partial_\eta - \partial_\chi$.

The convergence $\kappa(\hat{\mathbf{n}})$ is defined as $\hat{\nabla}^2\Psi(\hat{\mathbf{n}}) = -2\kappa(\hat{\mathbf{n}})$ and it is further related to density fluctuations along the geodesic by Poisson's equation [Eq. (7)]

$$\kappa(\hat{\mathbf{n}}) = \int_0^{\chi_s} d\chi(\nabla^2 - \nabla_\chi^2)\psi[r(\chi)\hat{\mathbf{n}}, \chi]\frac{r(\chi_s-\chi)r(\chi)}{r(\chi_s)} = \frac{3H_0^2}{2}\Omega_m\int_0^{\chi_s} d\chi\frac{\delta[r(\chi)\hat{\mathbf{n}}, \chi]}{a(\chi)}\frac{r(\chi_s-\chi)r(\chi)}{r(\chi_s)}. \quad (21)$$

The contribution from the radial derivatives ∇_χ^2 is proportional to the potential difference between the source and observer, and this boundary term is negligible compared to the first term [42,43]. Numerical ray tracing experiments through N-body simulations show that the weak lensing approximation to the first order in perturbations is accurate even in nonlinear regime when nonlinear matter power spectrum is used in place of linear matter power spectrum [42]. Also note that all the prior results for a single source redshift can be readily generalized to a source population with a redshift distribution $W(\chi_s)$ by integrating the results over χ_s with $W(\chi_s)$ in the integrand.

While conservation of surface brightness guarantees that photons are neither destroyed nor created, gravitational deflection distorts the cross section of a bundle of light rays, magnifying (or demagnifying) observed fluxes. Gravitational lensing magnification $\mu(\hat{\mathbf{n}})$ is related to the Jacobian of a mapping from the image plane to the source plane by

$$\mu(\hat{\mathbf{n}})^{-1} = \left|\frac{d^2\hat{\mathbf{s}}}{d^2\hat{\mathbf{n}}}\right| = |\mathbf{I} + \hat{\nabla}\hat{\nabla}\Psi(\hat{\mathbf{n}})| = |[1-\kappa(\hat{\mathbf{n}})]^2 - \gamma^2(\hat{\mathbf{n}})|, \quad (22)$$

where $\mathbf{I}$ is a unit 2×2 matrix and $\gamma(\hat{\mathbf{n}})$ is the tangential shear. In the weak lensing regime, $\mu(\hat{\mathbf{n}}) = 1 + 2\kappa(\hat{\mathbf{n}})$.

Gravitational lensing also modifies the propagation time of light rays in two ways, compared to the light travel time in the absence of the gravitational lensing effects: it distorts the photon geodesic, increasing the path length that photons travel, and the gravitational potential retards the light travel time. The former is referred to as the geometric time delay [44]

$$\tau_{\rm geo}(\hat{\mathbf{n}}) = \frac{1}{2}\frac{r(\chi_l)r(\chi_s)}{r(\chi_s-\chi_l)}\hat{\nabla}\Psi(\hat{\mathbf{n}})\cdot\hat{\nabla}\Psi(\hat{\mathbf{n}}), \quad (23)$$

and the latter is the potential or Shapiro time delay [45]

$$\tau_{\rm pot}(\hat{\mathbf{n}}) = \frac{r(\chi_l)r(\chi_s)}{r(\chi_s-\chi_l)}\Psi(\hat{\mathbf{n}}). \quad (24)$$

These effects can be derived by using the small angle approximation in deflection and the relation $d\eta = (1 - \psi + \phi)d\chi$ from the metric in Eq. (1). Note that the proper time delay can be obtained by multiplying the lens redshift $1 + z_l$ in the limit of a single lens case, and this derivation in a cosmological context recovers the standard relation for time delay.

III. SOURCE FLUCTUATIONS

Inhomogeneous matter fluctuations in the Universe deflect the propagation of light rays, giving rise to the gravitational lensing effects. The generalized Sachs-Wolfe effect also arises from the same matter fluctuations responsible for the gravitational lensing effects. Having discussed the basic mechanism of the gravitational lensing and the generalized Sachs-Wolfe effects that complicate the simple interpretation of observable quantities, we now investigate their impact on an observed overdensity field $\delta_{\rm obs}(\hat{\mathbf{n}}, z)$ of source galaxies. Contributions to $\delta_{\rm obs}(\hat{\mathbf{n}}, z)$ come from matter fluctuations in addition to the intrinsic overdensity $\delta(\hat{\mathbf{n}}, z)$ of source galaxies. Noting that the contributions can be linearized and added to the first order in perturbations, we separate these contributions as two physically distinct parts: one that involves the change of volume, and one that involves the intrinsic properties of source galaxies. The impact on galaxy two-point statistics will be discussed in the following section.

A. Volume effect

Consider a unit comoving volume $dV = r^2(\chi)d\Omega dz/H(z)$ and a unit flux interval df, and let $n(\hat{\mathbf{n}}, z, f)$ be the comoving number density of source galaxies. The generalized Sachs-Wolfe effect alters the unit comoving volume dV. Note, however, that it not only changes the unit redshift interval dz, but also changes both the angular diameter distance $r(\chi)$ and the Hubble parameter $H(z)$. By imposing the number conservation, the observed number density of the source galaxies can be

obtained by

$$n_{\rm obs}(z_{\rm obs}) = n(z)[1+\delta V]\frac{r^2(\chi)}{r^2(\chi_{\rm obs})}\frac{H(z_{\rm obs})}{H(z)}\frac{dz}{dz_{\rm obs}}, \quad (25)$$

where $\delta V = (2\phi+\varepsilon)_o^e$ represents the distortion of volume element, when it is transformed from the conformal Newtonian gauge to the local Lorentz frame, where the velocity of nonrelativistic matter vanishes. We give a more rigorous derivation in Appendix B. The solid angle $d\Omega$ remains unaffected by the generalized Sachs-Wolfe effect.

If the mean comoving number density evolves slowly compared to the redshift change due to the generalized Sachs-Wolfe effect $\bar{n}(z) = \bar{n}(z_{\rm obs})$, contributions to $\delta_{\rm obs}(z_{\rm obs})$ arise solely from the change in volume element dV,

$$\delta_{\rm obs}(z_{\rm obs}) = \delta(z) - 2\frac{1+z}{H\chi}\varepsilon - (1+z)H\frac{d}{dz}\left(\frac{\varepsilon}{H}\right) - \varepsilon + \delta V, \quad (26)$$

where we rewrote Eq. (16) as $1+z_{\rm obs} = (1+z)(1+\varepsilon)$ and the contribution ε from the generalized Sachs-Wolfe effect is

$$\varepsilon(z) = V(z) - V(0) - \psi(z) + \psi(0) - 2\int_0^\chi d\chi\frac{\partial\psi}{\partial\eta}. \quad (27)$$

In the Einstein-de Sitter universe, the Newtonian potential is constant and hence the integrated Sachs-Wolfe effect vanishes. In general, as we show in the next section, the peculiar velocity effect is dominant over the Sachs-Wolfe and the integrated Sachs-Wolfe effects, and $\varepsilon(z) \simeq V(z) - V(0)$. Note that while our derivation so far is valid for nonflat universes, in deriving Eq. (26) we assumed that the spatial curvature K is close to zero. The second term in Eq. (26) has a multiplicative factor $\sqrt{K}\chi/\tan(\sqrt{K}\chi)$ for a closed universe $K>0$ and $\sqrt{-K}\chi/\tanh(\sqrt{-K}\chi)$ for an open universe $K<0$, which becomes a unity as $K\to 0$.

With a proper line-of-sight distance $r_p = \chi(z)/(1+z)$ and a normalized peculiar velocity $u = V(z)/H(z)$, Eq. (26) can be rearranged as

$$\delta_{\rm obs}(z_{\rm obs}) = \delta(z) - \frac{2u}{r_p} - \frac{du}{dr_p}, \quad (28)$$

if we ignore the Sachs-Wolfe and the integrated Sachs-Wolfe effects in Eq. (27). This recovers the standard relation for redshift-space distortions [20,46,47]. Note that the standard method ignores the contributions in Eq. (26) from the Sachs-Wolfe and the integrated Sachs-Wolfe effects. We discuss their impact in Sec. IV.

Gravitational lensing magnification increases the flux interval df and the solid angle $d\Omega$ by a factor of μ, respectively. With the number conservation in dV and df, the observed number density is therefore

$$n_{\rm obs}(f_{\rm obs}) = n(f)\frac{df}{df_{\rm obs}}\frac{d\Omega}{d\Omega_{\rm obs}} = \frac{1}{\mu^2}n(f). \quad (29)$$

Similarly, if the mean comoving number density is the same over the flux change due to lensing magnification (i.e., the source luminosity function is flat), the observed overdensity is then

$$\delta_{\rm obs}(\hat{\mathbf{n}}) = \delta(\hat{\mathbf{n}}) - 4\kappa(\hat{\mathbf{n}}), \quad (30)$$

reflecting the change in volume and flux.

Gravitational lensing displaces the source position on the sky according to Eq. (19), and the observed number density is $n_{\rm obs}(\hat{\mathbf{n}}) = n[\hat{\mathbf{n}} + \hat{\nabla}\Psi(\hat{\mathbf{n}})]$. By Taylor expanding $n_{\rm obs}(\hat{\mathbf{n}})$ to the first order in $\Psi(\hat{\mathbf{n}})$, the observed overdensity can be written as

$$\delta_{\rm obs}(\hat{\mathbf{n}}) = \delta(\hat{\mathbf{n}}) + \hat{\nabla}\Psi(\hat{\mathbf{n}})\cdot\hat{\nabla}\delta(\hat{\mathbf{n}}). \quad (31)$$

Note that the additional contribution is already in the second order in perturbations and furthermore it vanishes on average, because the deflection angle $\hat{\nabla}\Psi(\hat{\mathbf{n}})$ has no preferred direction. The first nonvanishing effect from gravitational lensing displacement comes in the second order in $\Psi(\hat{\mathbf{n}})$ [31], and we therefore ignore this effect.

Finally the gravitational time delay decreases the arrival time of photons in an overdense region, compared to that in the absence of lensing. The net effect is therefore that we sample sources at farther distance in the fixed time interval [48]. However, for discrete sources the effect vanishes as long as the lifetime of the sources is longer than the time delay.

B. Source effect

The generalized Sachs-Wolfe and the gravitational lensing effects modify a unit volume and a unit flux interval, leading to the contributions to $\delta_{\rm obs}(\hat{\mathbf{n}}, z, f)$. Furthermore, the changes in observed redshift and flux can result in different mean number densities, if the redshift distribution of the source galaxy population varies in the redshift interval or the luminosity function is nontrivial over the flux change. These additional contributions from the change in mean number densities are related to the intrinsic properties of source galaxies, and we collectively refer to these effects as the source effect. However, note that while the source effect may be absent for some galaxy populations, the volume effect is always present. Therefore, we keep together the contributions from the volume effect in considering the source effect.

We first consider the effect of gravitational lensing magnification. Lensing magnification not only increases $d\Omega$ and df in Eq. (29), but also changes the number count of source galaxies, if the luminosity function is nonflat, i.e., $\bar{n}_{\rm obs}(f_{\rm obs}) \neq \bar{n}(f)$. Assuming $\bar{n}(f)df \propto f^{-s}df$ with a constant slope s over a narrow flux range df, the observed number density can be expressed as

$$\bar{n}_{\rm obs}(f_{\rm obs}) = \frac{\bar{n}(f_{\rm obs}/\mu)}{\mu^2} = \bar{n}(f_{\rm obs})\mu^{s-2}, \quad (32)$$

and the observed overdensity is now

$$\delta_{\rm obs}(\hat{\mathbf{n}}) = \delta(\hat{\mathbf{n}}) + (2s-4)\kappa(\hat{\mathbf{n}}) = \delta(\hat{\mathbf{n}}) + 5(p-0.4)\kappa(\hat{\mathbf{n}}), \quad (33)$$

where we used the logarithmic slope $p = d\log\bar{n}(m)/dm = 0.4(s-1)$ in a sample with limiting magnitude m. In the literature, these contributions from both the volume and the source effects are referred to as the magnification bias [27,49–52]. Note that this bias can be either positive or negative, depending on the slope p, and the volume effect can be canceled by the source effect with $p = 0.4$ (see [28] for the recent detection from the Sloan Digital Sky Survey).

The redshift distribution of source galaxies also affects the mean number counts due to the generalized Sachs-Wolfe effect. For a redshift distribution $\bar{n}(z)dz \propto z^\alpha \exp[-(z/z_0)^\beta]dz$, the observed overdensity can be obtained by substituting $\bar{n}(z)$ with $\bar{n}[z_{\rm obs} - (1+z_{\rm obs})\varepsilon]$,

$$\delta_{\rm obs}(z) = \delta(z) - \frac{1+z}{z}\left[\alpha - \beta\left(\frac{z}{z_0}\right)^\beta\right]\varepsilon - 2\frac{1+z}{H\chi}\varepsilon - (1+z)H\frac{d}{dz}\left(\frac{\varepsilon}{H}\right) - \varepsilon + \delta V, \quad (34)$$

where the second term in the right-hand side is the additional contribution related to the evolution of source galaxies, and the rest of the additional terms come from the volume effect in Eq. (26).

C. Summary

We have investigated the effects of inhomogeneous matter fluctuations on observed overdensity fields. Here we summarize their contributions and clarify the functional dependence. We then compare their impact on galaxy two-point statistics in Sec. IV.

For a sample of galaxies at redshift z selected with a limiting flux f and narrow intervals of dz and df, the observed overdensity $\delta_{\rm obs}(\hat{\mathbf{n}}, z, f)$ is the sum of the intrinsic overdensity field $\delta(\hat{\mathbf{n}}, z, f)$ and the contributions from the gravitational lensing and the generalized Sachs-Wolfe effects:

$$\delta_{\rm obs}(\hat{\mathbf{n}}, z, f) = \delta + \delta_{\rm mb} + \delta_z + \delta_{\rm evo}. \quad (35)$$

From Eq. (33), the magnification bias is defined as

$$\delta_{\rm mb}(\hat{\mathbf{n}}, z, f) = 5[p(f) - 0.4]\kappa(\hat{\mathbf{n}}, z), \quad (36)$$

with redshift z being the source redshift of the convergence $\kappa(\hat{\mathbf{n}})$ in Eq. (21). Considering $\varepsilon(z) \simeq V(z) - V(0)$, we call the volume effect in Eq. (26) as the redshift-space distortion bias,

$$\delta_z(\hat{\mathbf{n}}, z) = -2\frac{1+z}{H\chi}\varepsilon - (1+z)H\frac{d}{dz}\left(\frac{\varepsilon}{H}\right) - \varepsilon + \delta V = -2\frac{1+z}{H\chi}\varepsilon + \frac{1+z}{H}\varepsilon\frac{dH}{dz} - \frac{1+z}{H}\frac{\partial\varepsilon}{\partial\chi} - \varepsilon + \delta V. \quad (37)$$

Note that the generalized Sachs-Wolfe effect $\varepsilon(z)$ implicitly depends on the direction $\hat{\mathbf{n}}$ via the line-of-sight velocity $V(z) = v_\alpha e^\alpha = \hat{\mathbf{n}}\cdot\mathbf{v}(\hat{\mathbf{n}}, z)$, but it is independent of the limiting flux f, provided that galaxies have no velocity bias (i.e., galaxies and matter follow the same velocity field). Finally, the evolution bias is defined from Eq. (34) as

$$\delta_{\rm evo}(\hat{\mathbf{n}}, z, f) = -\frac{1+z}{z}\left[\alpha - \beta\left(\frac{z}{z_0}\right)^\beta\right]\varepsilon, \quad (38)$$

where the directional dependence comes from ε and the evolution coefficients (α, β, z_0) depend on the galaxy sample selected with the limiting flux f. While the evolution bias arising from the difference between $\bar{n}(z)$ and $\bar{n}(z_{\rm obs})$ was recognized [20,22,47], it has been ignored in the literature. However, we show in Sec. IV that the evolution bias can be significantly enhanced. Last, we want to emphasize that Eq. (35) is gauge invariant as is written in the conformal Newtonian gauge.

IV. GALAXY TWO-POINT STATISTICS

We have derived additional contributions of the gravitational lensing and the generalized Sachs-Wolfe effects to the intrinsic density fluctuations in Sec. III, fully consistent up to the first order in perturbations. Given two samples of galaxies with limiting fluxes f_1 and f_2, the observed galaxy correlation function is then $\xi_{\rm obs}(\hat{\mathbf{n}}_1, z_1, \hat{\mathbf{n}}_2, z_2) = \langle\delta_{\rm obs}(\hat{\mathbf{n}}_1, z_1)\delta_{\rm obs}(\hat{\mathbf{n}}_2, z_2)\rangle$ and the observed power spectrum is $\langle\delta_{\rm obs}(\mathbf{k}_1, z_1)\delta^*_{\rm obs}(\mathbf{k}_2, z_2)\rangle = (2\pi)^3\delta^D(\mathbf{k}_1 - \mathbf{k}_2)P_{\rm obs}(k_1)$. In Sec. IV A, we derive this ensemble average of all the combinations of each component in $\delta_{\rm obs}$ in Eq. (35), after we simplify the equation. We then discuss their impact on the observed galaxy two-point statistics by analyzing specific examples in Sec. IV B.

A. Correlation function and power spectrum

Here we compute the observed galaxy correlation function $\xi_{\rm obs}$ and power spectrum $P_{\rm obs}$. However, as some components in $\delta_{\rm obs}$ are smaller than other components, their combinations are even smaller by an order of magnitude. We therefore start by estimating the autocorrelation functions of each component and simplify the equation before we compute all the cross correlation functions and power spectra.

We first consider the correlation of the redshift-space distortion bias $\xi_{zz} = \langle\delta_z(\hat{\mathbf{n}}_1, z_1)\delta_z(\hat{\mathbf{n}}_2, z_2)\rangle$. The redshift-space distortion bias δ_z in Eq. (37) has five components that depend on either $\varepsilon(z)$ or its partial derivative with respect to z or χ, and the contribution $\varepsilon(z)$ from the

generalized Sachs-Wolfe effect in Eq. (27) has also three different components that depend on the peculiar velocity, the Newtonian potential, and its time derivative. The Newtonian potential and the peculiar velocity in Eqs. (7) and (8) take the simple form in Fourier space

$$\psi_{\mathbf{k}} = -\frac{3H_0^2}{2}\frac{\Omega_m}{a}\frac{\delta_{\mathbf{k}}}{k^2}, \tag{39}$$

$$\mathbf{v}_{\mathbf{k}} = iHfa\delta_{\mathbf{k}}\frac{\mathbf{k}}{k^2}. \tag{40}$$

On a typical correlation scale $1/k$, they scale as $H^2\delta_k/k^2$ and $H\delta_k/k$ with $f \simeq 1$ at $z \gtrsim 1$: ψ_k is smaller than v_k by the ratio of the correlation scale $1/k$ to the Hubble distance $1/H$. Similarly, the integrated Sachs-Wolfe effect is of the same order as the Newtonian potential and it vanishes in the limit of zero cosmological constant, i.e., Einstein-de Sitter universe, because it is proportional to the time derivative of the ratio of the growth factor to the expansion scale factor $D(z)/a$. Therefore, we can safely ignore the Sachs-Wolfe and the integrated Sachs-Wolfe effects and we assume $\varepsilon(z) \simeq V(z)$. Note that given a particular realization of the observer's rest frame, its peculiar velocity $V(0)$ is uncorrelated and the unobservable potential $\psi(0)$ in Eq. (27) can be absorbed by a gauge transformation.

With the assumption $\varepsilon(z) \simeq V(z)$, we further simplify Eq. (37) by comparing the five components in the redshift-space distortion bias, and similar justification was made in [30]. Respectively, each component scales as $\delta_k/k\chi$, $H\delta_k/k$, $\partial\delta_k/k\partial\chi$, $H\delta_k/k$, and $H\delta_k/k$, and hence they are smaller than δ_k by the ratio of correlation scale $1/k$ to the Hubble distance $1/H$ or the line-of-sight distance χ (roughly of order $1/H$), except the third component: the partial derivative with respect to χ cancels the correlation scale $1/k$ and hence the amplitude of the third component is of order δ_k, larger than the other components in the redshift-space distortion bias. Therefore, we only keep the dominant component in the redshift-space distortion bias [30],

$$\delta_z(\hat{\mathbf{n}}, z) \simeq -\frac{1+z}{H}\frac{\partial V}{\partial\chi}, \tag{41}$$

consistent with the standard relation for the redshift-space distortion, justifying its nomenclature. However, note that all these ignored components are proportional to ε. At low redshift, they contribute to galaxy two-point statistics at the subpercent level, while we show in Sec. IV B that at higher redshift their contribution is somewhat larger.

Having substantially reduced the number of combinations for an ensemble average, we are now well positioned to compute correlation functions and their power spectra. For two galaxy positions $\mathbf{x}_1 = [r(\chi_1)\hat{\mathbf{n}}_1, \chi_1]$ and $\mathbf{x}_2 = [r(\chi_2)\hat{\mathbf{n}}_2, \chi_2]$, the autocorrelation of the redshift-space distortion bias is

$$\begin{aligned}\xi_{zz} &= \langle\delta_z(\hat{\mathbf{n}}_1, z_1)\delta_z(\hat{\mathbf{n}}_2, z_2)\rangle \\ &= f_1 f_2\int\frac{d^3\mathbf{k}}{(2\pi)^3}e^{i\mathbf{k}\cdot(\mathbf{x}_1-\mathbf{x}_2)}P_m(k; z_1, z_2)\frac{k_z^4}{k^4} \\ &= f_1 f_2\int_0^\infty\frac{dk}{k}\frac{k^3}{2\pi^2}P_m(k; z_1, z_2)\Big[\frac{1}{5}j_0(kr_3)P_0(\gamma) \\ &\quad -\frac{4}{7}j_2(kr_3)P_2(\gamma)+\frac{8}{35}j_4(kr_3)P_4(\gamma)\Big],\end{aligned} \tag{42}$$

where the 3D comoving separation is $r_3 = [r(\bar{\chi})^2\Delta\theta^2 + (\chi_2-\chi_1)^2]^{1/2}$ with $\Delta\theta = |\hat{\mathbf{n}}_1 - \hat{\mathbf{n}}_2|$ and $\bar{\chi} = (\chi_1+\chi_2)/2$, and the angle subtended by the comoving separation is $\gamma = \cos\Delta\theta = (\chi_2-\chi_1)/r_3$. $P_n(x)$ and $j_n(x)$ are the n-th order Legendre polynomial and spherical Bessel function, respectively. We assumed the distant observer approximation such that k_z is the line-of-sight component of the wave number k, but it can be relaxed by replacing k_z^4 by $[(\hat{\mathbf{n}}_1\cdot\mathbf{k})(\hat{\mathbf{n}}_2\cdot\mathbf{k})]^2$. The linear matter power spectrum is computed by $P_m(k; z_1, z_2) = D(z_1)D(z_2)P_m(k)$, while we use $P_m(k; z_1, z_2) = P_m(k; \bar{z})$ with $\bar{z} = (z_1+z_2)/2$ when we compute the effect of the nonlinear matter power spectrum using the Smith *et al.* [53] approximation. The power spectrum of the redshift-space distortion bias can be readily read off from Eq. (42) and its power is boosted along the line-of-sight by $f_1 f_2\mu_k^4$ with $\mu_k = k_z/k$.

Next we consider the correlation of the evolution bias. The observed redshift $z_{\rm obs}$ is different from the true redshift z due to the generalized Sachs-Wolfe effect and the redshift distribution of the source mean number density gives rise to the evolution bias. The evolution bias $\delta_{\rm evo}$ is proportional to $\varepsilon(z) \simeq V(z)$ and it is typically smaller than δ_z by the ratio of a correlation scale $1/k$ to the Hubble distance $1/H$. However, beyond the mean redshift of source populations, the mean number density changes exponentially and the evolution bias can be substantially boosted by the prefactor

$$E(z; f) = -\frac{1+z}{z}\Big[\alpha - \beta\Big(\frac{z}{z_0}\Big)^\beta\Big], \tag{43}$$

defined such that Eq. (38) becomes $\delta_{\rm evo} = E(z)\varepsilon(z)$. While the exact functional form of $E(z)$ depends on the assumed redshift distribution, it captures the general trend of the enhancement in $\delta_{\rm evo}$ beyond the mean redshift. The correlation of the evolution bias is therefore

$$\begin{aligned}\xi_{\rm evo} &= \langle\delta_{\rm evo}(\hat{\mathbf{n}}_1, z_1)\delta_{\rm evo}(\hat{\mathbf{n}}_2, z_2)\rangle \\ &= (HfaE)_1(HfaE)_2\int\frac{d^3\mathbf{k}}{(2\pi)^3}e^{i\mathbf{k}\cdot(\mathbf{x}_1-\mathbf{x}_2)}P_m(k; z_1, z_2)\frac{k_z^2}{k^4} \\ &= (HfaE)_1(HfaE)_2\int_0^\infty\frac{dk}{k}\frac{k}{2\pi^2}P_m(k; z_1, z_2) \\ &\quad\times\Big[\frac{1}{3}j_0(kr_3)P_0(\gamma)-\frac{2}{3}j_2(kr_3)P_2(\gamma)\Big],\end{aligned} \tag{44}$$

where the subscripts in the round brackets represent that the products $(HfaE)$ are computed at z_1 and z_2. Its power

spectrum is also anisotropic and has structure similar to the redshift-space distortion bias.

Finally, the inhomogeneous matter fluctuations along the two lines-of-sight result in the correlation of the magnification bias

$$\begin{aligned}\xi_{\rm mb} &= \langle \delta_{\rm mb}(\hat{\mathbf{n}}_1, z_1)\delta_{\rm mb}(\hat{\mathbf{n}}_2, z_2)\rangle \\ &= (5p_1 - 2)(5p_2 - 2)\left(\frac{3H_0^2}{2}\Omega_m\right)^2 \int_0^{\chi_1} d\chi \left[\frac{r(\chi)}{a(\chi)}\right]^2 \\ &\quad \times \frac{r(\chi_1 - \chi)}{r_1}\,\frac{r(\chi_2 - \chi)}{r_2}\, w_p[r(\chi)\Delta\theta; z], \end{aligned} \tag{45}$$

where we used the Limber approximation [54] (see Appendix A). Without loss of generality, we assumed $z_1 \leq z_2$. The projected correlation function $w_p(R)$ is obtained by integrating the 3D matter correlation function $\xi_m(x)$ along the line-of-sight at a fixed redshift $z(\chi)$ and 2D transverse separation R,

$$\begin{aligned} w_p[R; z] &= \int_{-\infty}^{\infty} dr_\parallel \xi_m[r_3 = \sqrt{R^2 + r_\parallel^2}; z] \\ &= \int_0^\infty \frac{kdk}{2\pi} P_m(k; z) J_0(kR), \end{aligned} \tag{46}$$

where $J_n(x)$ is the n-th order Bessel function of the first kind. Assuming that the source redshifts are sufficiently high and hence $\xi_{\rm mb}$ is independent of z_1 and z_2, the power spectrum of the magnification bias is $P_{\rm mb} = (2\pi)\delta^D(k_z) \times (5p_1 - 2)(5p_2 - 2) r^2(\bar{\chi}) C^{\kappa\kappa}_{l=k_\perp r(\bar{\chi})}$, where the angular power spectrum of the convergence is

$$C_l^{\kappa\kappa} = \left(\frac{3H_0^2}{2}\Omega_m\right)^2 \int_0^{\bar{\chi}} d\chi \left[\frac{r(\bar{\chi} - \chi)}{a(\chi) r(\bar{\chi})}\right]^2 P_m\left[k = \frac{l}{r(\chi)}; z\right]. \tag{47}$$

The Dirac delta function results from our assumption that $\xi_{\rm mb}$ is a function of transverse direction only, but it can be somewhat relaxed by replacing $(2\pi)\delta^D(k_z)$ by a survey window function [55]. Note that while we are interested in how the magnification bias affects the 3D correlation of the intrinsic source fluctuations, the magnification bias arises from the matter fluctuations along the line-of-sight (not at a single redshift plane) and thereby angular correlation function and its angular power spectrum are better suited for quantifying its statistics. Indeed, the correlation function of the magnification bias is identical to the angular correlation function, $\xi_{\rm mb}(\hat{\mathbf{n}}_1, z_1, \hat{\mathbf{n}}_2, z_2) = w_{\rm mb}(\Delta\theta; z_1, z_2)$, and we relate 2D angular power spectrum to 3D power spectrum by $P(k) = (2\pi)\delta^D(k_z) r^2(\bar{\chi}) C_{l=k_\perp r(\bar{\chi})}$ (see Appendix A).

With all the additional contributions of the gravitational lensing and the generalized Sachs-Wolfe effects in hand, the correlation of the intrinsic fluctuation of sources is modeled using the linear bias model,

$$\begin{aligned}\xi_{\rm int} &= \langle \delta(\hat{\mathbf{n}}_1, z_1)\delta(\hat{\mathbf{n}}_2, z_2)\rangle \\ &= b_1 b_2 \int \frac{d^3\mathbf{k}}{(2\pi)^3} e^{i\mathbf{k}\cdot(\mathbf{x_1} - \mathbf{x_2})} P_m(k; z_1, z_2) \\ &= b_1 b_2 \int_0^\infty \frac{dk}{k}\frac{k^3}{2\pi^2} P_m(k; z_1, z_2) j_0(kr_3), \end{aligned} \tag{48}$$

where the constant linear bias factors b_1 and b_2 are the ratio of the intrinsic source fluctuation to the underlying matter fluctuation at z_1 and z_2.

To complete our calculations of $\xi_{\rm obs}$, we now compute the cross correlation functions and power spectra between the intrinsic source fluctuation and the fluctuations from the gravitational lensing and the generalized Sachs-Wolfe effects. First, the redshift-space distortion bias and the intrinsic source fluctuation provide two cross correlation functions

$$\begin{aligned}\xi_{\delta z} &= \langle \delta(\hat{\mathbf{n}}_1, z_1)\delta_z(\hat{\mathbf{n}}_2, z_2)\rangle \\ &= b_1 f_2 \int \frac{d^3\mathbf{k}}{(2\pi)^3} e^{i\mathbf{k}\cdot(\mathbf{x_1} - \mathbf{x_2})} P_m(k; z_1, z_2)\frac{k_z^2}{k^2} \\ &= b_1 f_2 \int_0^\infty \frac{dk}{k}\frac{k^3}{2\pi^2} P_m(k; z_1, z_2) \\ &\quad \times \left[\frac{1}{3} j_0(kr_3) P_0(\gamma) - \frac{2}{3} j_2(kr_3) P_2(\gamma)\right], \end{aligned} \tag{49}$$

and similarly for $\xi_{z\delta} = \langle \delta_z(\hat{\mathbf{n}}_1, z_1)\delta(\hat{\mathbf{n}}_2, z_2)\rangle$ with the two indices exchanged in Eq. (49). Combined with ξ_{zz} in Eq. (42), these two cross correlation functions constitute the standard redshift-space correlation function

$$\xi_{z-\rm dist} = \xi_{\rm int} + \xi_{zz} + \xi_{z\delta} + \xi_{\delta z} = \sum_{l=0,2,4} P_l(\gamma)\xi_l(r_3), \tag{50}$$

which is often expressed in terms of the multipole components [21,47,56]

$$\xi_l = c_l(\beta_1, \beta_2) b_1 b_2 i^l \int_0^\infty \frac{dk}{k}\frac{k^3}{2\pi^2} P_m(k; z_1, z_2) j_l(kr_3), \tag{51}$$

with its coefficients

$$\begin{pmatrix} c_0 \\ c_2 \\ c_4 \end{pmatrix} = \begin{pmatrix} 1 + \frac{\beta_1 + \beta_2}{3} + \frac{\beta_1\beta_2}{5} \\ \frac{2}{3}(\beta_1 + \beta_2) + \frac{4}{7}\beta_1\beta_2 \\ \frac{8}{35}\beta_1\beta_2 \end{pmatrix}, \tag{52}$$

where $\beta = f/b$. Analogously, the redshift-space power spectrum is

$$\begin{aligned} P_{z-\rm dist} &= P_{\rm int} + P_{z\delta} + P_{\delta z} + P_{zz} \\ &= [1 + (\beta_1 + \beta_2)\mu_k^2 + \beta_1\beta_2\mu_k^4] P_{\rm int}(k) \\ &= \sum_{l=0,2,4} P_l(\mu_k) P_l^z(k), \end{aligned} \tag{53}$$

with the intrinsic source power spectrum $P_{\rm int}(k) = b_1 b_2 P_m(k; z_1, z_2)$, and its multipole components $P_l^z(k)$ in Fourier space are related to the multipole components $\xi_l(r_3)$ in real space as

$$P_l^z(k) = 4\pi i^l \int_0^\infty dx x^2 \xi_l(x) j_l(kx). \tag{54}$$

Since the magnification bias arises from the matter fluctuations along the line-of-sight, it correlates with the intrinsic source fluctuation at lower redshift ($z_1 < z_2$),

$$\begin{aligned}\xi_{\delta\rm mb} &= \langle \delta(\hat{\mathbf{n}}_1, z_1)\delta_{\rm mb}(\hat{\mathbf{n}}_2, z_2)\rangle \\ &= b_1(5p_2 - 2)\left(\frac{3H_0^2}{2}\Omega_m\right) \\ &\quad \times \frac{r(\chi_2 - \chi_1) r_1}{a_1 r_2} w_p[r_1 \Delta\theta; z_1],\end{aligned} \tag{55}$$

but the correlation vanishes when the source is at higher redshift, i.e., $\xi_{{\rm mb}\delta} = 0$. The power spectrum is also related to the angular power spectrum of the cross term

$$\begin{aligned}C_l^{\delta\rm mb} &= b_1(5p_2 - 2)\left(\frac{3H_0^2}{2}\Omega_m\right)\frac{r(\chi_2 - \chi_1)}{a_1 r_1 r_2} \\ &\quad \times P_m\left[k_\perp = \frac{l}{r_1}; z_1\right],\end{aligned} \tag{56}$$

as $P_{\delta\rm mb} = (2\pi)\delta^D(k_z) r_1^2 C^{\delta\rm mb}_{l=k_\perp r_1}$. Finally, all the cross correlations that involve $\delta_{\rm evo}$ are zero, since $\delta_{\rm evo}$ is odd in the line-of-sight component V of peculiar velocities and the Universe has no preferred direction. Two remaining cross terms $\xi_{z\rm mb}$ and $\xi_{{\rm mb}z}$ also vanish, since δ_z is proportional to k_z^2 and the line-of-sight fluctuations are smoothed out in the Limber approximation.

B. Comparison

To compare the additional contributions to the observed correlation function $\xi_{\rm obs}$ and power spectrum $P_{\rm obs}$, we consider near-future dark energy surveys that will target galaxies and quasars to measure their correlation function and power spectrum at high redshifts. For example, the baryonic oscillation spectroscopic survey (BOSS) will measure 1.5×10^6 luminous red galaxies to determine the angular diameter distances at $z = 0.35$ and 0.6, and use 160 000 quasars to measure the clustering of Lyman-α forests at $z = 2.5$ [57,58]. For the purpose of illustration, we show our calculations of galaxy two-point statistics at these redshifts. Here we adopt a flat ΛCDM universe: the cosmological parameters are the matter density $\Omega_m h^2 = 0.137$, the baryon density $\Omega_b h^2 = 0.0227$, the Hubble constant $h = 0.70$, the spectral index $n_s = 0.96$, the optical depth to the last scattering surface $\tau = 0.084$, and the primordial curvature perturbation amplitude $\Delta_\zeta^2 = 2.457 \times 10^{-9}$ at $k = 0.002$ Mpc^{-1} (corresponding to the matter power spectrum normalization $\sigma_8 = 0.817$), consistent with the recent results (e.g., [33–35]). The matter transfer function is computed by using CMBFAST [59].

Figure 1 examines the separate contributions of the gravitational lensing and the generalized Sachs-Wolfe effects to the observed two-point correlation function of galaxies. We show the correlation functions of the intrinsic galaxy fluctuations ($\xi_{\rm int}/b^2$; *solid line*) and the redshift-space distortion bias (ξ_{zz}; *dotted line*), and their cross correlation function ($\xi_{\delta z}/b = \xi_{z\delta}/b$; *long dashed line*). The correlation functions are computed by using the linear (*thin line*) and the nonlinear (*thick line*) matter power spectrum. Note that they only differ on small scales and the nonlinear effect decreases at high redshift as shown in Fig. 1(a) to Fig. 1(c), going from $z = 0.35$ to $z = 2.5$. The source galaxies are assumed to be at the same redshift ($z = z_1 = z_2$) shown in the figure legend, and thus 3D separation r_3 is equal to 2D projected separation $R = r(\bar{\chi})\Delta\theta$. However, two galaxy populations are separately placed at $z_1 = 0.35$ and $z_2 = 0.6$ in Fig. 1(d), and the x axis represents projected separation R, rather than 3D separation r_3.

The solid lines $\xi_{\rm int}/b^2$ are identical to the matter correlation function ξ_m and the linear bias factor b is constant. However, the nonlinear evolution and galaxy formation process complicate the relation between galaxies and underlying matter fluctuations, and galaxy bias becomes scale dependent on small scales, even when the nonlinear matter power spectrum is used (e.g., [60,61]). While we plot the correlation functions at $r_3 \simeq 0.5 - 200h^{-1}$ Mpc for completeness, the validity of our calculation is limited to the linear regime. The solid lines at $r_3 = 151$ Mpc ($= 106h^{-1}$ Mpc) show prominent enhancement in the clustering amplitude, known as the baryonic acoustic peak [62,63]. The baryon-photon plasma in the early Universe propagates as sound waves and these periodic oscillations in Fourier space translate into one peak in real space with its width deviating from a sharp delta function due to the termination of the harmonic series, determined by the horizon size at the cosmological recombination epoch. Note that the correlation function becomes negative at $r_3 \simeq 128h^{-1}$ Mpc, beyond which we plot its absolute value.

The correlation functions (ξ_{zz}, $\xi_{\delta z}$, and $\xi_{z\delta}$) of the redshift-space distortion bias have the overall shape similar to $\xi_{\rm int}$. However, since ξ_{zz}, $\xi_{\delta z}$, and $\xi_{z\delta}$ in Eqs. (42) and (49) have additional functional dependence on spherical Bessel functions $j_2(x)$ and $j_4(x)$ compared to $\xi_{\rm int}$ in Eq. (48), it puts more weight on higher k and hence the nonlinear effects persist up to $r_3 \simeq 10h^{-1}$ Mpc in Fig. 1(a), larger than $3h^{-1}$ Mpc for $\xi_{\rm int}$. However, the incoherent superposition of the additional Bessel functions washes out the acoustic peak in the correlation functions of the redshift-space distortion bias, leaving little structure in ξ_{zz}, $\xi_{\delta z}$, and $\xi_{z\delta}$ at the acoustic scale. Since the observed correlation function $\xi_{\rm obs}$ is the sum of all the contributions and it is hard in practice to separate each contribution from

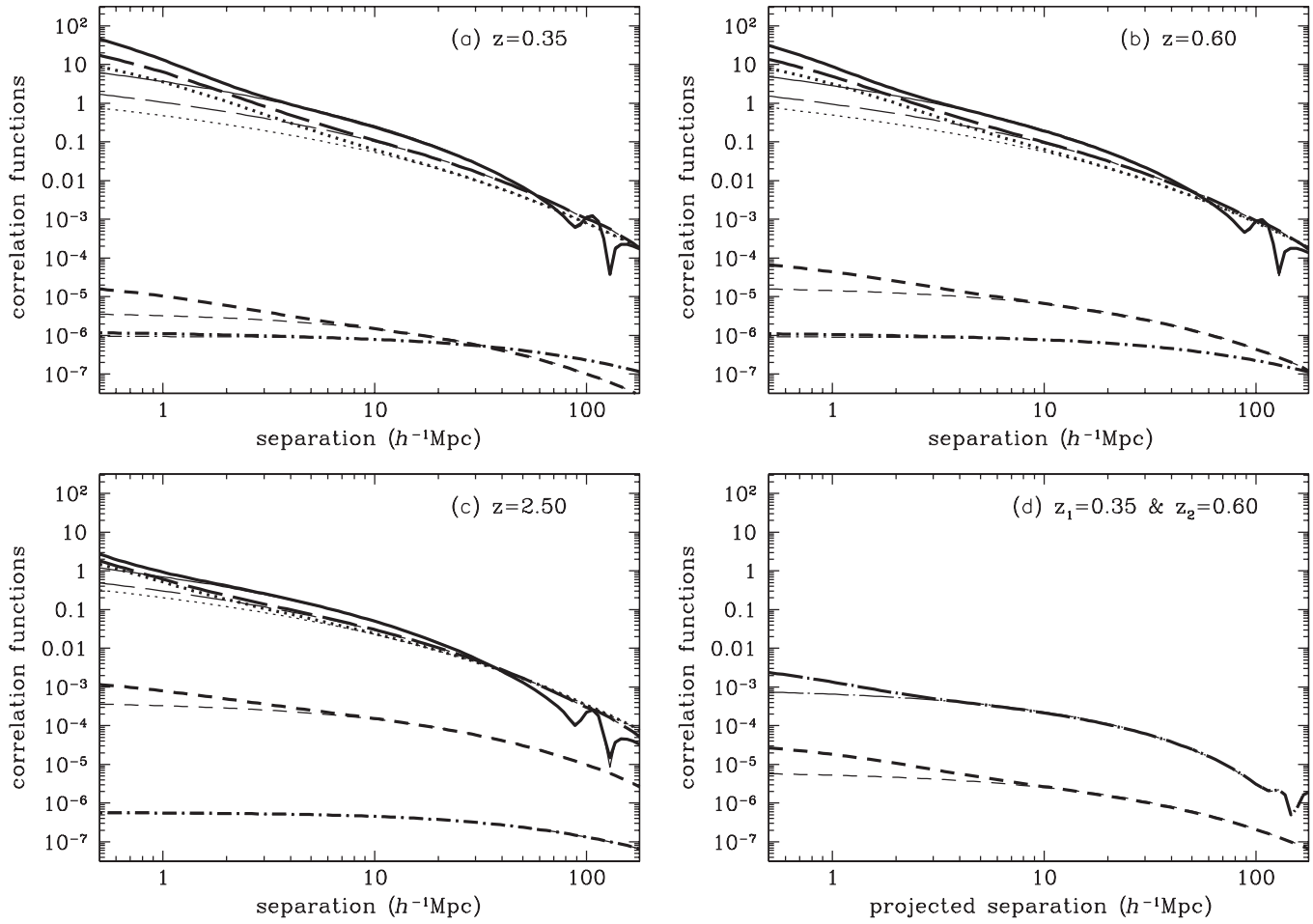

FIG. 1. Dissection of the observed two-point correlation function of galaxies. Solid, dotted, and long dashed lines represent correlation functions of the intrinsic source fluctuations $\xi_{\rm int}/b^2$ and the redshift-space distortion bias ξ_{zz}, and their cross correlation function $\xi_{\delta z}/b = \xi_{z\delta}/b$, respectively. Correlation functions of the magnification bias $\xi_{\rm mb}/(5p-2)^2$ and the evolution bias $\xi_{\rm evo}/E^2$ are shown as short dashed and short dot-dashed lines. Note that while the galaxy bias factor b and magnification bias factor $(5p-2)$ are of order unity, the evolution boost factor E can be an order of magnitude larger (see Fig. 3). The correlation functions are computed by using the linear (*thin line*) and the nonlinear (*thick line*) matter power spectra, and source galaxies are assumed to be at the same redshift indicated in the legend. The correlation functions of the intrinsic source fluctuations become negative at $r_3 \gtrsim 128h^{-1}$ Mpc, where its absolute value is plotted. Panel (*d*) plots the cross correlation function $\xi_{\delta\rm mb}/b_1(5p_2-2)$ of the intrinsic fluctuation of source galaxies at $z_1 = 0.35$ and the magnification bias from source galaxies at $z_2 = 0.6$ as long dot-dashed lines. With large line-of-sight separation $600h^{-1}$ Mpc, only $\xi_{\rm mb}$ and $\xi_{\delta\rm mb}$ that depend on projected separation R rather than 3D separation r_3 itself are appreciable, i.e., $\xi_{\rm int} \simeq \xi_{\delta z} \simeq \xi_{z\delta} \simeq \xi_{zz} \simeq \xi_{\rm evo} \simeq 0$.

one another, it may look as if $\xi_{\rm int}$ is swamped by ξ_{zz}, $\xi_{\delta z}$, and $\xi_{z\delta}$ at the acoustic scale, but note that we plot $\xi_{\rm int}/b^2$ and $\xi_{\delta z}/b$: the linear bias factor of luminous red galaxies is $b_0 \simeq 1.5$–2.0 [9,10,12,64]. Assuming that galaxies have no velocity bias $\mathbf{v}_g = \mathbf{v}$, the linear bias factor at high redshift is $b(z) - 1 = (b_0 - 1)/D(z)$, sufficient for $\xi_{\rm int}$ to show its structure, when combined with ξ_{zz}, $\xi_{\delta z}$, and $\xi_{z\delta}$, yet the plot without b captures the main structure of the correlation functions, since the linear bias factor is still of order unity.

Note that since the source galaxies are at the same redshift in Fig. 1(a) to Fig. 1(c), the cosine angle of the comoving separation is $\gamma = (\chi_2 - \chi_1)/r_3 = 0$, i.e., the redshift-space correlation function (the sum of the solid, dotted, and dashed lines) is $\xi_{z-\rm dist} = \xi_{\rm int} + \xi_{zz} + \xi_{z\delta} + \xi_{\delta z} = \xi_0 - (1/2)\xi_2 + (3/8)\xi_4$, different from the angle-averaged (monopole) correlation ξ_0 often used in the literature [65,66]. Figure 2 illustrates the multipole components of the redshift-space correlation function at $z = 0.35$. The monopole (*solid line*) is identical to $\xi_{\rm int}$ in shape but differs in normalization by $\xi_0 = \xi_{\rm int} \cdot c_0$ with the multipole coefficient c_0 in Eq. (52). The quadrupole ξ_2 (*dotted line*) is negative by the sign convention and the hexadecapole ξ_4 (*dashed line*) is positive in the figure, while the monopole ξ_0 changes its sign as $\xi_{\rm int}$ changes at $r_3 \gtrsim 128h^{-1}$ Mpc (see the inset). As noted before, the spherical Bessel functions $j_2(kr_3)$ and $j_4(kr_3)$ in ξ_2 and ξ_4 peak at

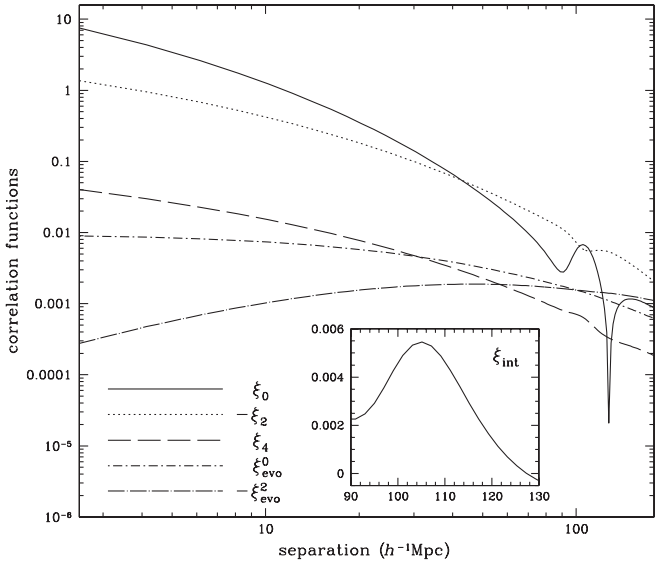

FIG. 2. Multipole components of the redshift-space correlation function $\xi_{z-\mathrm{dist}}$ and the evolution bias ξ_{evo} at $z = 0.35$. We define multipole components of ξ_{evo} as $\xi_{\mathrm{evo}} = \xi^0_{\mathrm{evo}}(r_3)P_0(\gamma) + \xi^2_{\mathrm{evo}}(r_3)P_2(\gamma)$, in the same way multipole components of $\xi_{z-\mathrm{dist}}$ are defined in Eq. (50). We assume that the galaxy bias factor is $b = 2$ and the evolution boost factor is $E = 100$ for a proper comparison. The correlation functions are computed by using the linear matter power spectrum only. $\xi_0(r_3)$ becomes negative at $r_3 \gtrsim 128h^{-1}$ Mpc, where its absolute value is plotted. The inset shows the correlation ξ_{int} of the intrinsic source fluctuations around the acoustic scale and it is related to the monopole by $\xi_0 = \xi_{\mathrm{int}} \cdot c_0$ in Eq. (51), where $c_0 = 1.24$ in our fiducial model.

scales different from the typical scale $k \sim 1/r_3$ for ξ_0, and thus the acoustic structure seen in ξ_0 is smoothed out in ξ_2 and ξ_4.

In practice, galaxy redshift surveys have a narrow but nonzero radial window function and galaxy pairs in the same redshift bin often have the line-of-sight separation comparable to the transverse separation, i.e., $\gamma \neq 0$. The angular dependence of the redshift-space correlation function, therefore, complicates the interpretation of its measurements, which are further plagued by low signal-to-noise ratios in estimates of ξ_2 and ξ_4. While the monopole ξ_0 can be used to ease the theoretical and/or observational challenge, full analysis of the anisotropic structure of $\xi_{z-\mathrm{dist}}$ could in principle bring more information than ξ_0 measurements (see [24,25] for recent analysis). We analyze the full anisotropic structure of the observed correlation function ξ_{obs} below. On small scales, virial motions of galaxies result in additional anisotropic structure in $\xi_{z-\mathrm{dist}}$, known as the Finger-of-God (FoG) effect. Note that since this effect involves galaxy motions in nonlinear objects, it is not considered in our calculation and linear theory provides an inaccurate description of the FoG effect: while a simple dispersion model [67] is often adopted to extract additional information contained in the anisotropic structure, it is demonstrated [68] that this model leads to an unphysical distribution of pairwise velocities. However, this difficulty could be tackled by recent approach based on modeling nonlinear galaxy bias in redshift-space [69–71].

The short dashed and short dot-dashed lines in Fig. 1 show the correlation functions of the magnification bias $\xi_{\mathrm{mb}}/(5p-2)^2$ and the evolution bias ξ_{evo}/E^2, respectively. The magnification bias ξ_{mb} is typically smaller than ξ_{int} by the ratio of the transverse correlation scale $1/k_\perp$ to the Hubble distance $1/H$, and the magnification bias factor is of order unity, $(5p-2) = -1.0 \sim 2.0$ [28] for galaxies and quasars, while it can be further suppressed by the source effect canceling the volume effect $(5p-2) \simeq 0$. Since ξ_{mb} in Eq. (45) is proportional to the projected correlation function w_p, its overall shape is similar to ξ_{int} but ξ_{mb} is positive due to projection of ξ_{int}. As the source population is located at higher redshift, longer line-of-sight distance increases the gravitational lensing effect and ξ_{mb} increases in redshift, as opposed to $\xi_{\mathrm{int}} \propto D^2 \propto 1/(1+z)^2$ decreasing in redshift. For example, ξ_{mb} at $z = 2.5$ in Fig. 1(c) can grow up to a few percent of ξ_{int} at the acoustic scale [31,32].

The evolution bias δ_{evo} is often ignored in the literature compared to the redshift-space distortion bias δ_z, since $\delta_{\mathrm{evo}} \propto \varepsilon \simeq V$ and $V \ll \delta_z$. However, the evolution bias can be significantly enhanced when the mean number density of sources changes rapidly in redshift. To estimate the evolution boost factor $E(z)$ in Eq. (43), we assume the standard functional form of a redshift distribution $\bar{n}(z)dz \propto z^\alpha \exp[-(z/z_0)^\beta]dz$ and take two source populations as illustrative examples: galaxies and quasars characterized by $(\alpha, \beta, z_0) = (4, 4, 0.4)$ and $(3, 13, 2)$, respectively [12,28,72]. While the bright samples of luminous red galaxies in the BOSS will have a redshift distribution flatter than the assumed here, the faint samples with larger number density and volume will have a nonflat redshift distribution [73,74]. The clustering of Lyman-α forests at $z = 2.5$ will be measured by the spectrum of quasars at $z > 2.5$, not by quasars themselves at $z = 2.5$. However, we simply assume that ξ_{obs} is measured from the galaxy samples at $z = 0.35$ and $z = 0.6$, and from the quasar samples at $z = 2.5$.

The upper panel of Fig. 3 illustrates the redshift distribution of the galaxy (*dashed line*) and quasar (*solid line*) samples, with its peak at $z = 0.4$ and 1.8, and the bottom panel shows the evolution boost factor $E(z)$ of each sample. For the assumed redshift distribution, the evolution boost factor is typically a factor $\sim$10, and it vanishes at the peak redshift. However, a sharp decline in the mean number density of source populations beyond the mean redshift makes the evolution bias δ_{evo} sensitive to the change in observed redshift z_{obs} due the generalized Sachs-Wolfe effect, and $E(z)$ can be further enhanced by another factor of 10. With significant boost of $E^2(z) \simeq 100$–10000, the correlation ξ_{evo} of the evolution bias should be given a

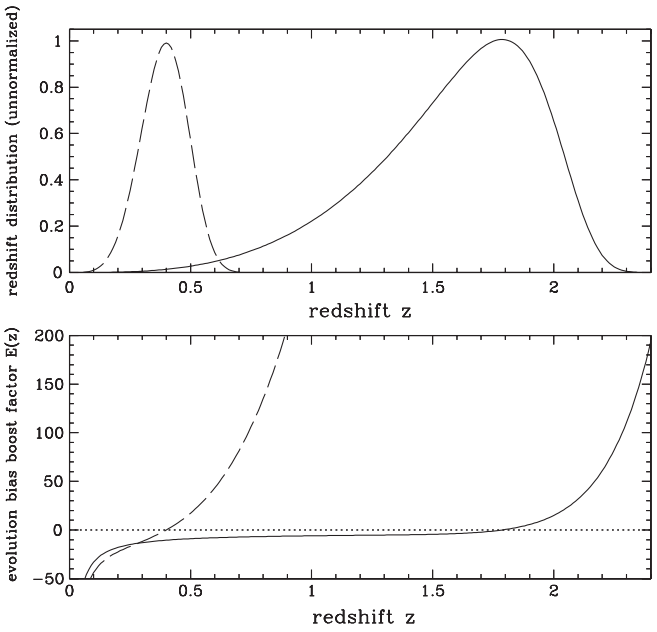

FIG. 3. Redshift distribution of source populations and boost factor $E(z)$ of the evolution bias. Assuming the standard functional form $\bar{n}(z)dz \propto z^{\alpha}\exp[-(z/z_0)^{\beta}]dz$, the redshift distribution of galaxies (*dashed line*) and quasars (*solid line*) are shown in the upper panel with $(\alpha, \beta, z_0) = (4, 4, 0.4)$ for galaxies and (3, 13, 2) for quasars, respectively [12,28,86]. The bottom panel shows the evolution bias boost factor computed by using Eq. (43). The number density of sources changes exponentially beyond the mean redshift and the evolution bias is substantially enhanced in proportion to $E(z)$.

proper consideration, especially when the mean number of the source population changes rapidly. Note that the evolution bias $\xi_{\rm evo}/E^2$ (*short dot-dashed line*) in Fig. 1(a) is comparable to the magnification bias $\xi_{\rm mb}/(5p-2)^2$ (*short dashed line*) and is larger at the acoustic peak scale, and the evolution boost factor $E(z)$ can be significantly larger than the magnification bias factor $(5p-2)$. Therefore, it is of particular importance to select samples of source populations that have relatively flat redshift distribution in number density ($E \simeq 10$), and to limit the redshift range of measurements below the peak redshift. The short and the long dot-dashed lines in Fig. 2 show the multipole components $\xi^l_{\rm evo}$ of the evolution bias, defined as $\xi_{\rm evo} = \sum_{l=0,2}\xi^l_{\rm evo}(r_3)P_l(\gamma)$. Both components are smooth and change little over $r_3 = 1 - 200h^{-1}$ Mpc. With $\xi_{\rm evo} \propto H^2a^2D^2 \propto 1/(1+z)$, it decreases slowly in redshift, and the nonlinear effect is relatively small compared to $\xi_{\rm int}$, since less weight is given to short wavelength modes.

Now recall that there are four terms of δ_z in Eq. (37) that are ignored in our calculation, and they are comparable to $\varepsilon \simeq V$, albeit smaller than the dominant term in $\delta_z \simeq -\frac{1+z}{H}\frac{\partial V}{\partial \chi}$. While there is no additional boost factor like $E(z)$ in $\delta_{\rm evo}$, their contributions to $\xi_{\rm obs}$ are typically of order $\xi_{\rm evo}/E^2$ and are as large as $\xi_{\rm mb}$ at $z = 0.35$ in Fig. 1(a). Though $\xi_{\rm mb}$ is larger at higher redshift, their impact on $\xi_{\rm obs}$ also increases in redshift: approximately at the subpercent level for each contribution at $z = 2.5$. This level of accuracy would be appropriate given the statistical errors present in current samples, but further calculations of the ignored terms may be needed in future surveys.

In Fig. 1(a), we consider the correlation functions of two source populations, separately located at $z_1 = 0.35$ and $z_2 = 0.6$ as a function of 2D projected separation $R = r(\bar{\chi})\Delta\theta$. Note that given a large line-of-sight separation $\sim 600h^{-1}$ Mpc between z_1 and z_2, all the correlation functions that depend on 3D comoving separation r_3 are nearly zero, i.e., $\xi_{\rm int} \simeq \xi_{\delta z} \simeq \xi_{z\delta} \simeq \xi_{zz} \simeq \xi_{\rm evo} \simeq 0$. The two nonvanishing contributions in Fig. 1(d) are the autocorrelation of the magnification bias $\xi_{\rm mb}/(5p_1-2)(5p_2-2)$ (*short dashed line*) and the cross correlation of the intrinsic source fluctuation and the magnification bias $\xi_{\delta{\rm mb}}/b_1(5p_2-2)$ (*long dot-dashed line*) that depend on the projected separation, rather than 3D separation itself. Note that the cross correlation in Fig. 1(a) to Fig. 1(c) is identically zero: $\xi_{\delta{\rm mb}} = 0$ at $z_1 = z_2$ with the Limber approximation we adopted here, but it is in general smaller than $\xi_{\rm mb}$ unless $z_1 \neq z_2$ (see [31] for a somewhat different derivation). Note that while both $\xi_{\rm mb}$ and $\xi_{\delta{\rm mb}}$ in Eqs. (45) and (55) depend on the projected separation via w_p, $\xi_{\delta{\rm mb}}$ has additional linear dependence on the comoving line-of-sight separation $\chi_2 - \chi_1 = \Delta\chi$, and it increases with $\Delta\chi$, as opposed to $\xi_{\rm mb}$ with little dependence on $\Delta\chi$. With the large $\Delta\chi \sim 600h^{-1}$ Mpc in Fig. 1(d), $\xi_{\delta{\rm mb}}$ is substantially larger than $\xi_{\rm mb}$.

Figure 4 examines the anisotropic structure of the observed correlation function $\xi_{\rm obs}$, evaluated at $\bar{z} = 0.35$. The x axis represents the transverse separation $R = r(\bar{\chi})\Delta\theta$ and the y axis represents the line-of-sight separation $\Delta\chi = \chi_2 - \chi_1$ with fixed $\bar{z} = (z_1+z_2)/2 = 0.35$, $\bar{\chi} = (\chi_1+\chi_2)/2 = 980h^{-1}$ Mpc, and $\chi(z_1) \le \chi(z_2)$. The color maps are linearly proportional to the value of the correlation function ξ plotted in each panel below the adopted threshold $\xi = 4\times10^{-4}$, and they are logarithmically proportional to ξ above the threshold. The solid contours are also logarithmically spaced with increasing thickness at $\xi \ge 1.5\times10^{-3}$ to emphasize the structure shown as the color maps, and their contour values are labeled in the color bar. The thickest solid contours separate the regions with $\xi > 0$ from those with $\xi < 0$, and the dot-dashed and dotted curves represent the contours with $\xi = -4.5\times10^{-4}$ and -9.0×10^{-4}, respectively. For reference, we also plot the acoustic scale in $\xi_{\rm int}$ ($r_3 = 106h^{-1}$ Mpc) as dashed lines in each panel. In Fig. 4(a), we plot the correlation function $\xi_{\rm int}$ of the intrinsic source fluctuations, assuming the galaxy bias factor $b = 2$. As the rings of the concentric contours show, $\xi_{\rm int}$ is spherically symmetric and depends only on 3D separation r_3. The acoustic peak shows its structure as a circular ring at $r_3 = 106h^{-1}$ Mpc (*dashed line*) and beyond $r_3 \sim 128h^{-1}$ Mpc

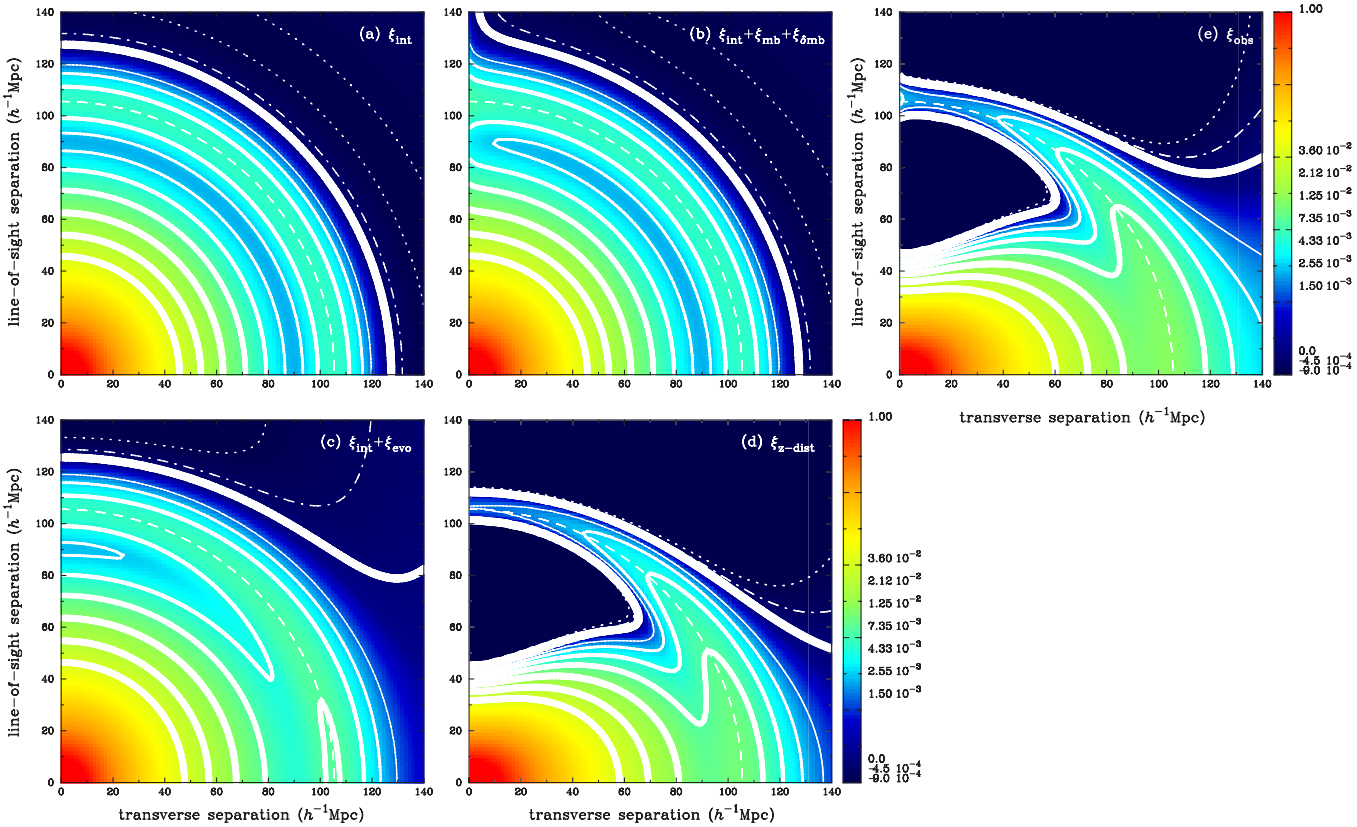

FIG. 4 (color online). Anisotropic structure of the observed correlation function $\xi_{\rm obs}$ at $z = 0.35$. We plot the correlation function $\xi_{\rm int}$ of the intrinsic source fluctuations in panel (a), and show the individual effects of the magnification bias $\xi_{\rm int} + \xi_{\rm mb} + \xi_{\delta\rm mb}$ [panel (b)], the evolution bias $\xi_{\rm int} + \xi_{\rm evo}$ [panel (c)], and the redshift-space distortion bias $\xi_{z-\rm dist} = \xi_{\rm int} + \xi_{zz} + \xi_{z\delta} + \xi_{\delta z}$ [panel (d)] on the anisotropic structure. The observed correlation function $\xi_{\rm obs}$, the sum of all the correlation functions, is shown in panel (e). We assume that the galaxy bias factor is $b = 2$, the magnification bias factor is $(5p - 2) = 2$, and the evolution boost factor is $E = 100$. The color maps are linearly proportional to the value of correlation function ξ in each panel at $\xi < 4 \times 10^{-4}$ and are logarithmically proportional to ξ at $\xi > 4 \times 10^{-4}$. The solid contours are logarithmically spaced at $\xi \geq 1.5 \times 10^{-3}$ and their thickness increases with the value of ξ (contour values are labeled in the color bar), while the thickest solid curves represent the $\xi = 0$ contour. The dot-dashed and dotted curves represent the contours with $\xi = -4.5 \times 10^{-4}$ and -9.0×10^{-4}, respectively. The acoustic scale in $\xi_{\rm int}$ ($r_3 = 106h^{-1}$ Mpc) is shown as dashed lines in each panel for reference. Note that two regions are underrepresented in the color maps, as the region with $\xi > 1.0$ is highly concentrated at $r_3 \ll 20h^{-1}$ Mpc and there is no distinctive feature in the anisotropic structure around the region with $\xi < 0$.

$\xi_{\rm int}$ becomes negative without further distinctive feature in its structure.

The gravitational lensing effects, the magnification bias $\xi_{\rm mb}$ and its cross correlation $\xi_{\delta\rm mb}$, break the spherical symmetry in $\xi_{\rm int}$, and its impact on the anisotropic structure is shown in Fig. 4(b), assuming the magnification bias factor $(5p - 2) = 2$. $\xi_{\rm mb}$ depends on the line-of-sight separation $\Delta\chi$ only through χ_1 and χ_2 in Eq. (45), and $\Delta\chi$ is small compared to the line-of-sight distance, i.e., $\Delta\chi \ll \chi_1 \simeq \chi_2$. Thus $\xi_{\rm mb}$ is virtually independent of $\Delta\chi$ and is just a function of transverse separation R, decreasing with increasing R. As is seen in Fig. 1(a), $\xi_{\rm mb}$ is in general orders of magnitude smaller than $\xi_{\rm int}$ at $z = 0.35$, but $\xi_{\rm int}$ becomes negative at large r_3 and smaller than $\xi_{\rm mb}$, e.g., $\xi_{\rm int} = -8.4 \times 10^{-4} < \xi_{\rm mb} = 4.8 \times 10^{-6}$ at $R = 10.0h^{-1}$ Mpc and $\Delta\chi = 140h^{-1}$ Mpc ($r_3 = 140.3h^{-1}$ Mpc). Since $\xi_{\rm mb}$ changes slowly with R, the demarcation curve between the regions with $\xi_{\rm mb} > \xi_{\rm int}$ and $\xi_{\rm mb} < \xi_{\rm int}$ roughly corresponds to the $\xi_{\rm int} = 0$ contour (*thickest solid line*) in Fig. 4(a). However, since $|\xi_{\rm int}| > \xi_{\rm mb}$ in general except at a narrow strip around the $\xi_{\rm int} = 0$ contour, the impact of $\xi_{\rm mb}$ on the anisotropic structure is negligible at $\bar{z} = 0.35$. Note that the impact of $\xi_{\rm mb}$ is substantially enhanced at higher redshift, where longer line-of-sight distance results in more fluctuations and the clustering amplitude of $\xi_{\rm int}$ is lower.

While both $\xi_{\rm mb}$ and $\xi_{\delta\rm mb}$ are proportional to w_p, $\xi_{\delta\rm mb}$ depends on w_p itself, rather than the integral of w_p along the line-of-sight, on which $\xi_{\rm mb}$ depends: $\xi_{\delta\rm mb}$ becomes negative at large transverse separation $R \simeq 110h^{-1}$ Mpc as $\xi_{\rm int}$ becomes negative at large 3D separation r_3. Note that for an observable angular separation $\Delta\theta$, the transverse

separation $R = r(\bar{\chi})\Delta\theta$ in the figure is slightly different from $r(\chi_1)\Delta\theta$ for w_p in Eq. (55), and this difference tilts otherwise a vertical line with $\xi_{\delta\mathrm{mb}} = 0$ at $R \simeq 110h^{-1}$ Mpc toward larger R at large $\Delta\chi$ ($\xi_{\delta\mathrm{mb}} = 0$ at $R \simeq 128h^{-1}$ Mpc and $\Delta\chi = 140h^{-1}$ Mpc), because $\Delta\chi = \chi_2 - \chi_1$ and $z_1 \le z_2$ with fixed $\bar{z} = (z_1 + z_2)/2 = 0.35$. Furthermore, since $\xi_{\delta\mathrm{mb}}$ linearly increases with $\Delta\chi$ (hence it vanishes at $\Delta\chi = 0$), the absolute value of $\xi_{\delta\mathrm{mb}}$ is larger than ξ_{mb} except at the regions at $\Delta\chi = 0$ and around the nearly vertical strip with $\xi_{\delta\mathrm{mb}} = 0$, and it is also comparable to ξ_{int} at large $\Delta\chi$ and small R, e.g., $\xi_{\delta\mathrm{mb}} = 4.3 \times 10^{-4}$ at $R = 10h^{-1}$ Mpc and $\Delta\chi = 140h^{-1}$ Mpc. Therefore, when ξ_{int} is combined with ξ_{mb} and $\xi_{\delta\mathrm{mb}}$ as shown in Fig. 4(b), ξ_{mb} has little impact but $\xi_{\delta\mathrm{mb}}$ distorts the symmetric contours of ξ_{int} at large $\Delta\chi$ and small R. At higher redshift, the amplitude of $\xi_{\delta\mathrm{mb}}$ decreases with that of ξ_{int}, and ξ_{mb} becomes a more dominant contribution than $\xi_{\delta\mathrm{mb}}$. Note that the amplitude at the acoustic scale (*dashed line*) is not significantly altered by the gravitational lensing effects, even along the line-of-sight direction at $\bar{z} = 0.35$.

The impact of the evolution bias ξ_{evo} is shown in Fig. 4(c), where we assume the evolution boost factor $E = 100$. While ξ^0_{evo} and ξ^2_{evo} change slowly with separation, they have the opposite sign as shown in Fig. 2. Therefore, they tend to cancel out along the line-of-sight direction ($\gamma = 1$), reducing the amplitude of ξ_{evo}, and the largest contribution of ξ_{evo} arises along the transverse direction ($\gamma = 0$), where the absolute values of the monopole ξ^0_{evo} and the quadrupole ξ^2_{evo} add up. For example, $\xi_{\mathrm{evo}} = 1.6 \times 10^{-3} > \xi_{\mathrm{int}} = -8.4 \times 10^{-4}$ at $R = 140h^{-1}$ Mpc and $\Delta\chi = 10h^{-1}$ Mpc. As noted in Fig. 1(a), the amplitude of ξ_{evo} with $E = 100$ is smaller than ξ_{int} at $r_3 < 50h^{-1}$ Mpc and its impact is appreciable only at $r_3 \ge 100h^{-1}$ Mpc along the transverse direction. As the angular separation becomes small with fixed 3D separation, the impact of ξ_{evo} decreases, because the second order Legendre polynomial is a monotonic function of angle. Note that compared to ξ_{int}, ξ_{evo} changes slowly in redshift and its impact is larger at higher redshift for a fixed E. The overall shape of the acoustic scale (*dashed line*) also remains unaffected by the evolution bias.

Figure 4(d) examines the redshift-space correlation function $\xi_{z-\mathrm{dist}} = \xi_{\mathrm{int}} + \xi_{zz} + \xi_{\delta z} + \xi_{z\delta}$. Though its angular structure is similar to ξ_{evo}, it differs in two aspects: $\xi_{z-\mathrm{dist}}$ has the additional hexadecapole ξ_4, and the quadrupole ξ_2 becomes dominant over the monopole ξ_0 at $r_3 \simeq 50h^{-1}$ Mpc smaller than $r_3 \simeq 200h^{-1}$ Mpc, where $\xi^0_{\mathrm{evo}} \simeq \xi^2_{\mathrm{evo}}$, shown in Fig. 2. Therefore, the angular structure changes more dramatically than that seen in Fig. 4(c). Note that while the fourth order Legendre polynomial is not a monotonic function of angle, the hexadecapole ξ_4 is generally smaller than ξ_0 and ξ_2, and its contribution is minor. The contours exhibits the well-known Kaiser effect [20] that coherent infall toward the overdense regions squashes the clustering amplitude and the underdense regions inflate along the line-of-sight. The large region with negative values at $\Delta\chi \simeq 50 - 100h^{-1}$ Mpc and $R \le 60h^{-1}$ Mpc is the characteristic feature of this effect, largely due to the negative quadrupole ξ_2, and this structure has been recently measured with high signal-to-noise ratio [24,25]. Even along the line-of-sight direction, the monopole ξ_0 briefly takes over the negative quadrupole around the acoustic scale, because the clustering amplitude is enhanced. Furthermore, while the clustering amplitude increases with angle at the acoustic scale (*dashed line*), its structure manifests itself as ridges [22].

Figure 4(e) puts together our discussion, plotting the observed correlation function ξ_{obs} at $\bar{z} = 0.35$, the sum of all the correlation functions shown in each panel. The redshift-space distortion affects the anisotropic structure by far the most among the other effects considered here. The gravitational lensing effects, mostly from $\xi_{\delta\mathrm{mb}}$ at low redshift, become important only at a small transverse but large line-of-sight separation. With the same dependence on quadrupole, ξ_{evo} follows the similar angular pattern of $\xi_{z-\mathrm{dist}}$, boosting their contributions along the transverse direction, but its sole impact shows up at $R \ge 110h^{-1}$ Mpc due to the lower amplitude. The clustering amplitude of ξ_{obs} at the acoustic scale (*dashed line*) is no longer constant, nor a monotonic function of angle. The peak location, imprinted in ξ_{int} with local enhancement in clustering amplitude, remains largely unaffected as the gravitational lensing and generalized Sachs-Wolfe effects distorts the anisotropic structure. However, note that it is beyond our scope of the current investigation to what accuracy the acoustic peak remains unaffected by these effects (see, e.g., [31,32,72,75–79] for recent work on the robustness of the baryonic acoustic peak).

Figure 5 shows the equivalent dissection of the contributions of the gravitational lensing and the generalized Sachs-Wolfe effects to the observed galaxy power spectrum P_{obs} in Fourier space. The solid, dashed, and dotted lines represent P_{int}/b^2, P_{evo}/E^2, and $P_{\mathrm{mb}}/(5p - 2)^2$, respectively. The power spectra are also computed by using the linear (*thin line*) and the nonlinear (*thick line*) matter power spectrum as in Fig. 1. In Fig. 5(a), the source galaxies are assumed to be at the same redshift ($z = z_1 = z_2$), and the two sets of lines show the power spectra at $z = 0.35$ and $z = 2.5$, which decrease in redshift except that P_{mb} increases as we have seen ξ_{mb} increase in redshift. The power spectrum of the intrinsic source fluctuations P_{int}/b^2 (*solid line*) exhibits two characteristic scales in its structure: a series of the acoustic oscillations starting at $k \simeq 0.085h$ Mpc^{-1}, and the turnover in the overall shape at $k \simeq 0.015h$ Mpc^{-1} imprinted by the horizon size at the matter-radiation equality $z = 3300$.

For simplicity, the wave number is set equal to the line-of-sight direction $k = k_z$ for plotting P_{evo} and to the transverse direction $k = k_\perp$ for plotting P_{mb}. The power spec-

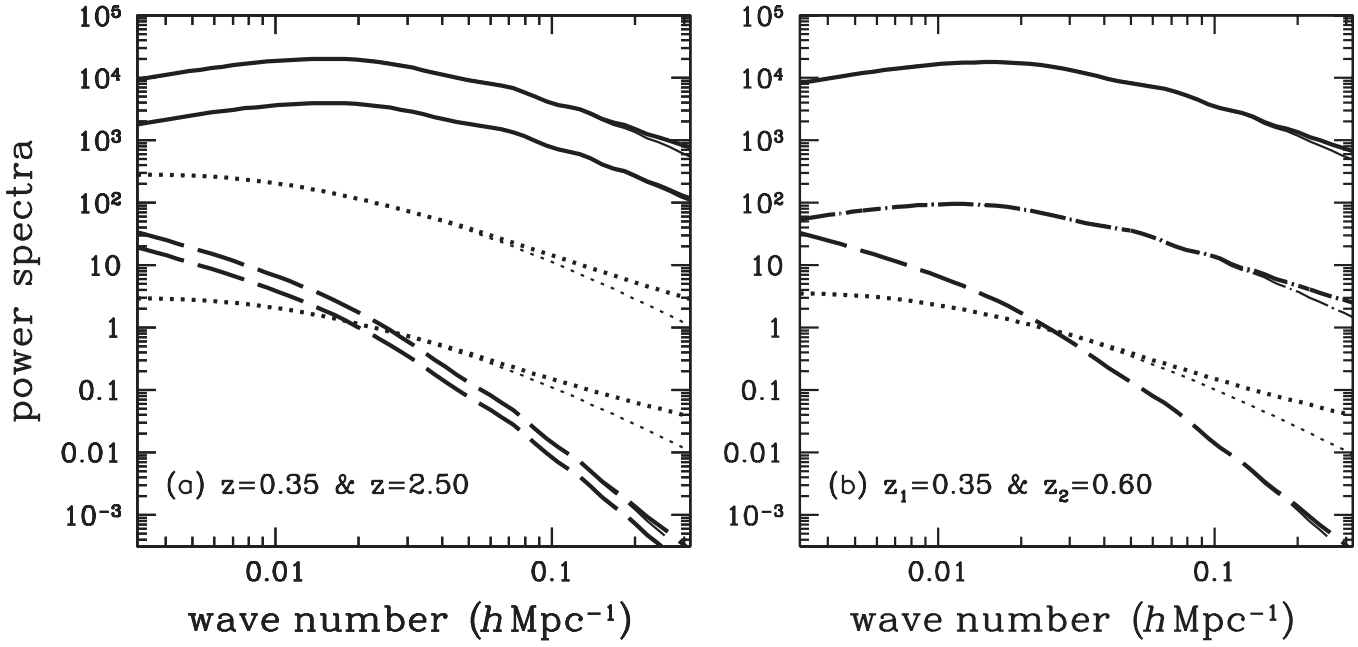

FIG. 5. Dissection of the observed galaxy power spectrum $P_{\rm obs}$. Solid and dashed lines represent power spectra of the intrinsic source fluctuations $P_{\rm int}/b^2$ and the evolution bias $P_{\rm evo}/E^2$. Power spectrum of the magnification bias $P_{\rm mb}/(5p-2)^2$ is shown as dotted lines for a survey window of width $200h^{-1}$ Mpc (see the text). Note that we omit power spectra of the redshift-space distortion bias P_{zz}, $P_{\delta z}$, and $P_{z\delta}$, since they have the same shape as $P_{\rm int}$ for the line-of-sight component of the wave number $k_z = k$ up to numerical factors of order unity. Thin and thick lines represent power spectra computed by using the linear and nonlinear matter power spectrum. *Left panel:* power spectra are computed at two different redshifts, only the power spectrum of the magnification bias increases at higher z, while $P_{\rm int}$ and $P_{\rm evo}$ decrease. *Right panel:* cross-power spectra are computed for two galaxy populations at $z_1 = 0.35$ and $z_2 = 0.6$, and dot-dashed lines show the cross-power spectrum of the intrinsic source fluctuation at z_1 and the magnification bias of source galaxies at z_2. Large line-of-sight separation $\sim 600h^{-1}$ Mpc corresponds to $k_z \simeq 0.002h$ Mpc^{-1} and it has little impact on power spectrum ($k \simeq k_\perp \gg k_z$).

trum of the evolution bias $P_{\rm evo}/E^2$ (*dashed line*) is typically many orders-of-magnitude smaller than $P_{\rm int}/b^2$ at $k \geq 0.03h$ Mpc^{-1} in Fourier space, but its contribution can be at the few percent level of $P_{\rm int}$ at the acoustic scale and comparable to $P_{\rm int}$ at the matter-radiation equality scale, with the evolution boost factor $E^2 \simeq 10000$. Note that the power spectra of the redshift-distortion bias P_{zz}, $P_{\delta z}$, and $P_{z\delta}$ are omitted in the figure, because they have the same shape as $P_{\rm int}$ up to numerical factors of order unity when $k = k_z$.

To plot the power spectrum of the magnification bias $P_{\rm mb}/(5p-2)^2$ (*dotted line*), we replace $(2\pi)\delta^D(k_z)$ by a flat window function of width $200h^{-1}$ Mpc, typical value in redshift surveys, hence the dotted line *de facto* delineates the angular power spectrum of the magnification bias $(5p-2)^2 C^{\kappa\kappa}_{l=k_\perp r(\bar\chi)}$ with a dimensional coefficient $r^2(\bar\chi) \times (200h^{-1}$ Mpc) (see Appendix A). While the magnification bias is negligible at $z = 0.35$, its effect increases with larger line-of-sight distance at higher redshift, amounting to a few percent at the acoustic scale and larger at the matter-radiation equality scale at $z = 2.5$. However, note that even with relatively large contributions to $P_{\rm obs}$, the shift in the peak positions can be at the subpercent level or smaller [31,32].

Figure 5(b) plots the cross power spectra of two source populations at $z_1 = 0.35$ and $z_2 = 0.6$. As opposed to the correlation functions shown in Fig. 1(d), all the power spectra that depend on 3D wave number remains virtually unaffected by the large line-of-sight separation $\sim 600h^{-1}$ Mpc, because it corresponds to very small wave number $k_z \simeq 0.002h$ Mpc^{-1} and $k \simeq k_\perp \gg k_z$. The dot-dashed lines show the cross power spectrum of the intrinsic source fluctuation and the magnification bias $P_{\delta\rm mb}$. Since it is proportional to the line-of-sight separation, its contribution is larger than $P_{\rm mb}$ in Fig. 5(b), but it is absent in Fig. 5(a).

The anisotropic structure of the observed power spectrum $P_{\rm obs}$ has been well studied with main focus on the effect of the redshift-space distortion bias [20], and the redshift-space power spectrum $P_{z-\rm dist}$ in Eq. (53) has the multipole components that are identical in shape but only differ in normalization. The evolution bias results in the similar angular pattern: two multipole components that share its shape with $P_{\rm int}$ with different normalization. However, note that since the magnification bias and its cross term are intrinsically 2D quantities, their impact on the anisotropic structure of $P_{\rm obs}$ is small, even with realistic survey window functions [55].

V. DISCUSSION

Galaxy two-point statistics, correlation function in real space, and power spectrum in Fourier space, have been extensively used in cosmology to characterize the underlying matter fluctuations. We have presented a coherent theoretical framework based on the linearized FLRW metric for computing the gravitational lensing and the generalized Sachs-Wolfe effects. Within this framework, the metric perturbations are sourced by the underlying matter fluctuations, and they naturally give rise to perturbations in the observable redshift of source galaxies and their angular position on the sky. The time component of the photon geodesic equations can be used to show the former, the generalized Sachs-Wolfe effect [40] that generalizes the standard redshift-space distortion by peculiar velocities in a cosmological context, including the Sachs-Wolfe and the integrated Sachs-Wolfe effects. The spatial components of the photon geodesic equations can be used to derive the latter, the gravitational lensing effect that includes the weak lensing distortion, magnification, and time delay effects. This unified treatment provides a complete description of the relation between these seemingly different effects and the underlying matter fluctuations.

Furthermore, it becomes transparent in this treatment how the gravitational lensing and the generalized Sachs-Wolfe effects affect the observed fluctuation field of source galaxies. To the linear order in perturbations, we have computed all the additional contributions to the intrinsic source fluctuation, arising from the gravitational lensing and the generalized Sachs-Wolfe effects. We can gain more insight on the impact of these effects by separating them as two physically distinct origins: the volume and the source effects. The former effect that involves the change of volume is independent of source galaxy populations and hence regardless thereof the volume effect is always present in galaxy two-point statistics. By contraries, the latter effect depends on the intrinsic properties of source galaxy populations and may vanish for a certain population. All of these contributions to the intrinsic source fluctuations result in numerous additional auto and cross terms in the observed galaxy two-point statistics, and therefore proper account should be taken into these additional terms in interpreting measurements of galaxy two-point statistics from upcoming dark energy surveys.

With the complete list of the contributions of the gravitational lensing and the generalized Sachs-Wolfe effects, separated as two physically distinct origins, we have identified several contributions in the volume effect and one contribution in the source effect, which are ignored in the standard treatment: the evolution bias in the source effect arises from the generalized Sachs-Wolfe effect, when the mean number density of sources changes rapidly in redshift, and its impact on the observed galaxy two-point statistics can be substantially larger than that of the gravitational lensing magnification bias. The ignored contributions in the volume effect are typically of order peculiar velocities and hence they are subdominant, compared to the standard redshift-space distortion effect. However, their impact is comparable to the magnification bias at low redshift. While the cross term of the magnification bias and the intrinsic source fluctuation is more important at low redshift than the contribution of the magnification bias itself in the gravitational lensing effect, further calculations of the additional contributions associated with the volume effect may be needed, if higher accuracy of theoretical modeling is required from observation.

We have investigated the impact of the additional contributions to the anisotropic structure of the observed galaxy two-point statistics, after simplifying some of the contributions to the intrinsic source fluctuations. The redshift-space distortion affects the observed galaxy two-point statistics most, imprinting its well-known feature in the anisotropic structure [20,46,47]. The gravitational lensing effect is small but non-negligible at a percent level, particularly along the line-of-sight separation and at high redshift, since their contribution increases with longer line-of-sight distance to the source galaxies and the clustering amplitude of the intrinsic source fluctuations decreases in redshift. The evolution bias has an angular pattern similar to the redshift-space distortion, but its impact becomes appreciable, only at fairly large transverse separation. While it is challenging to analyze the observed anisotropic structure of galaxy two-point statistics, its full analysis from upcoming dark energy surveys can provide a great opportunity to separately identify each contribution from the gravitational lensing and the generalized Sachs-Wolfe effects, increasing the leverage to understand the underlying physical mechanism.

However, we note that constraining the underlying cosmological model will require not only accurate theoretical predictions, but also model fitting to measurements, which results in further distortion in galaxy two-point statistics, known as Alcock-Paczyński effect [80]. Furthermore, our current investigation has focused on the linear theory predictions and its additional contributions: nonlinearity and scale-dependent galaxy bias can affect our results, though its impact is expected to be less than at the percent level around the acoustic scale (see, e.g., [75–77]). However, additional leverage can be gained by modeling scale-dependent galaxy bias on nonlinear scales [81].

ACKNOWLEDGMENTS

We acknowledge useful discussions with Jordi Miralda-Escudé. We are very grateful to Matias Zaldarriaga and Liam Fitzpatrick for discussions of the effect of volume distortion. J. Y. is supported by the Harvard College Observatory under the Donald H. Menzel fund.

APPENDIX A: 2D AND 3D STATISTICS

Here we derive the relation between 2D and 3D fluctuations and their two-point statistics. Consider a fluctuation field $\delta^{2D}(\hat{\mathbf{n}}; z_s)$ on the sky from a source population at z_s. In general, it can be expressed in terms of the convolution of a window function $W(\chi)$ and its 3D fluctuation $\delta^{3D}(\mathbf{x})$

$$\delta^{2D}(\hat{\mathbf{n}}; z_s) = \int_0^\infty d\chi W(\chi_s - \chi)\delta^{3D}[r(\chi)\hat{\mathbf{n}}, \chi; z]. \quad \text{(A1)}$$

When the window function is appreciable only around z_s representing a narrow selection function in redshift surveys, $\delta^{2D}(\hat{\mathbf{n}}; z_s) \simeq \delta^{3D}(\mathbf{x}; z_s)$ with its functional dependence $\mathbf{x} = [r(\chi_s)\hat{\mathbf{n}}, \chi_s]$. However, contributions to $\delta^{2D}(\hat{\mathbf{n}}; z_s)$ can come from the fluctuations $\delta^{3D}(\mathbf{x}; z)$ at $z < z_s$ and $\delta^{2D}(\hat{\mathbf{n}}; z_s)$ may be substantially different from $\delta^{3D}(\mathbf{x}; z_s)$, when the window function is broad. For example, the convergence field $\kappa(\hat{\mathbf{n}}; z_s)$ in Eq. (21) has the window function

$$W^\kappa(\chi_s - \chi) = \left(\frac{3H_0^2}{2}\Omega_m\right)\frac{r(\chi_s - \chi)r(\chi)}{a(\chi)r(\chi_s)}, \quad \text{(A2)}$$

which peaks roughly at a half of $r(\chi_s)$.

In a sufficiently small patch of the sky, the Fourier mode of $\delta^{2D}(\hat{\mathbf{n}}; z_s)$ is

$$\begin{aligned}\delta_l^{2D}(z_s) &= \int d^2\hat{\mathbf{n}} e^{-i\boldsymbol{l}\cdot\hat{\mathbf{n}}}\delta^{2D}(\hat{\mathbf{n}}; z_s) \\ &= \int_0^\infty d\chi \frac{W(\chi_s - \chi)}{r^2(\chi)}\int\frac{dk_z}{2\pi}e^{ik_z\chi}\delta^{3D} \\ &\quad\times\left[k_z, \mathbf{k}_\perp = \frac{\boldsymbol{l}}{r}; z\right], \end{aligned} \quad \text{(A3)}$$

and its (angular) power spectrum is

$$\begin{aligned}C_l(z_1, z_2) &= \int\frac{d^2\boldsymbol{l}\boldsymbol{l}}{(2\pi)^2}\langle\delta_l^{2D}(z_1)\delta_{l'}^{2D*}(z_2)\rangle \\ &= \int d\chi_a\int d\chi_b\frac{W(\chi_1 - \chi_a)W(\chi_2 - \chi_b)}{r(\chi_a)^2} \\ &\quad\times\int\frac{dk_z}{2\pi}e^{ik_z(\chi_a - \chi_b)}P\left[k_z, k_\perp = \frac{l}{r(\chi_a)}; z_a, z_b\right] \\ &= \int d\chi\frac{W(\chi_1 - \chi)W(\chi_2 - \chi)}{r^2(\chi)}P\left[k = \frac{l}{r(\chi_a)}; z\right]. \end{aligned} \quad \text{(A4)}$$

The last equality is obtained by adopting the Limber approximation, in which fluctuations along the line-of-sight are smoothed out and only long wavelength modes ($k_z \simeq 0$) can contribute to the integral [54,82]. With the Limber approximation, the angular correlation function is

$$\begin{aligned}w(\Delta\theta; z_1, z_2) &= \langle\delta^{2D}(\hat{\mathbf{n}}_1; z_1)\delta^{2D}(\hat{\mathbf{n}}_2; z_2)\rangle \\ &= \int_0^\infty d\chi W(\chi_1 - \chi)W(\chi_2 - \chi) \\ &\quad\times w_p[r(\chi)\Delta\theta; z], \end{aligned} \quad \text{(A5)}$$

where the projected correlation function is

$$\begin{aligned}w_p[R; z] &= \int_{-\infty}^\infty dr_\parallel\xi[r = \sqrt{R^2 + r_\parallel^2}; z] \\ &= \int_0^\infty\frac{kdk}{2\pi}P(k; z)J_0(kR). \end{aligned} \quad \text{(A6)}$$

The angular correlation function and power spectrum in Eqs. (45) and (47) can be readily obtained by substituting the window function $W^\kappa(\chi)$ for the convergence in Eq. (A2) with $W(\chi)$ in Eqs. (A4) and (A5). The cross correlation function and power spectrum in Eqs. (55) and (56) can be computed in a similar manner, since $W(\chi_s - \chi) = \delta^D(\chi_s - \chi)$ gives $\delta^{2D}(\hat{\mathbf{n}}; z_s) = \delta^{3D}(\mathbf{x}; z_s)$.

In Sec. IV, we associated the angular power spectrum $C_l^{\kappa\kappa}$ to a 3D power spectrum to compare its impact with other 3D power spectra. A 3D fluctuation field can be constructed from $\delta^{2D}(\hat{\mathbf{n}}; z_s)$ by

$$\begin{aligned}\delta(\mathbf{k}; z_s) &= \int d^3\mathbf{x}e^{-i\mathbf{k}\cdot\mathbf{x}}\delta^{2D}(\hat{\mathbf{n}}; z_s) \\ &= \int d\chi_s r^2(\chi_s)e^{-ik_z\chi_s}\delta^{2D}_{l=\mathbf{k}_\perp r_s}(z_s) \\ &= (2\pi)\delta^D(k_z)r^2(\chi_s)\delta^{2D}_{l=\mathbf{k}_\perp r_s}(z_s). \end{aligned} \quad \text{(A7)}$$

We assumed δ_l^{2D} is independent of z_s in the last equality. For high redshift source populations, this approximation is accurate, since the growth of the comoving angular diameter distance flattens at high z and it becomes nearly constant. Within this approximation $r(\chi_1) = r(\chi_2) = r(\bar{\chi})$, the 3D power spectrum is anisotropic and it is related to the angular power spectrum by

$$\begin{aligned}P(k_z, k_\perp; z_1, z_2) &= \int\frac{d^3\mathbf{k}'}{(2\pi)^3}\langle\delta(\mathbf{k}; z_1)\delta^*(\mathbf{k}'; z_2)\rangle \\ &= (2\pi)\delta^D(k_z)r^2(\bar{\chi})C_{l=k_\perp r(\bar{\chi})}(\bar{z}). \end{aligned} \quad \text{(A8)}$$

In practice, $\delta^D(k_z)$ need to be replaced by a survey window function [55], but note that it is crucial to assume the independence of source redshift, when computing the power spectrum. We also note that the Limber approximation breaks down when the radial window function of a survey is narrow compared to the correlation length scale (see, e.g., [83,84]). However, the use of the Limber approximation is readily justified in galaxy surveys, in which the radial window function has width of $\Delta z \simeq 0.1$–0.2, corresponding to several hundred Mpc.

APPENDIX B: GAUGE-INVARIANT FORM OF OBSERVED NUMBER DENSITY

Here we provide a rigorous derivation of the observed number density in Sec. III A. For simplicity, we assume a flat universe.

In the observer's frame, local coordinates p^α are used to describe the observed positions of galaxies and their true positions are related to the observed positions by the

photon geodesic $x^a(\lambda)$. The total number of observed galaxies can be computed by considering a covariant volume integral [85]:

$$N_{\rm gal} = \int \sqrt{-g} n_{\rm phy} u^d dS_d, \tag{B1}$$

where the (oriented) hypersurface element is

$$dS_d = \epsilon_{abcd} \frac{\partial x^a}{\partial p^1} \frac{\partial x^b}{\partial p^2} \frac{\partial x^c}{\partial p^3} dp^1 dp^2 dp^3, \tag{B2}$$

g is the determinant of the spacetime metric, $n_{\rm phy}$ is the physical number density of galaxies, and $\epsilon_{abcd} = \epsilon_{[abcd]}$ is the Levi-Civita tensor density. We take the Newtonian gauge variables $(\tilde{z}, \tilde{\theta}, \tilde{\phi})$ as the observed local coordinates p^α. For notational simplicity, tilde is used to represent observed quantities (e.g., $\tilde{z} = z_{\rm obs}$). By imposing the number conservation, the observed number density is then related to the total number of galaxies by

$$N_{\rm gal} = \int \tilde{n} \frac{\chi^2(\tilde{z})}{H(\tilde{z})} \sin\tilde{\theta} d\tilde{z} d\tilde{\theta} d\tilde{\phi}. \tag{B3}$$

In a homogeneous universe, the local coordinates are identical to the true coordinates $(\tilde{z}, \tilde{\theta}, \tilde{\phi}) = (z, \theta, \phi)$, and the photon geodesic is simply $x^a(\lambda) = (y, ye^\alpha)$, where we choose the normalization of the affine parameter as $\lambda = (a/\nu)y$. Noting that the four velocity of a comoving observer is $u^a = (1/a, 0)$, Eq. (B1) can be readily solved as

$$\begin{aligned} N_{\rm gal} &= \int a^4 \frac{n_{\rm phy}}{a} \epsilon_{\alpha\beta\gamma 0} \frac{\partial x^\alpha}{\partial \tilde{z}} \frac{\partial x^\beta}{\partial \tilde{\theta}} \frac{\partial x^\gamma}{\partial \tilde{\phi}} d\tilde{z} d\tilde{\theta} d\tilde{\phi} \\ &= \int a^3 n_{\rm phy} \frac{\chi^2(z)}{H(z)} \sin\theta dz d\theta d\phi. \end{aligned} \tag{B4}$$

Therefore, we recover the standard relation for $N_{\rm gal}$ and $\tilde{n} = a^3 n_{\rm phy} = n(z, \theta, \phi)$.

In an inhomogeneous universe, the photon geodesic deviates from the null path and the local coordinates are different from the true coordinates. Perturbations to the photon geodesic in an inhomogeneous universe can be computed by integrating the null vector $k^a(\lambda) = dx^a/d\lambda$,

$$x^a(\lambda) = (y, ye^\alpha) + \int_0^y dy' (\delta\nu, \delta e^\alpha). \tag{B5}$$

Note that to the first order in perturbations the integration is performed along the null path, ranging from the observer at $y = 0$ to the source galaxies at y.

With $u^a = ((1 - \psi)/a, v^\alpha/a)$, the integrand of Eq. (B1) is

$$\begin{aligned} u^d dS_d = &\frac{1 - \psi}{a} \epsilon_{\alpha\beta\gamma 0} \frac{\partial x^\alpha}{\partial \tilde{z}} \frac{\partial x^\beta}{\partial \tilde{\theta}} \frac{\partial x^\gamma}{\partial \tilde{\phi}} \\ &+ \frac{v^\alpha}{a} \epsilon_{abc\alpha} \frac{\partial x^a}{\partial \tilde{z}} \frac{\partial x^b}{\partial \tilde{\theta}} \frac{\partial x^c}{\partial \tilde{\phi}}. \end{aligned} \tag{B6}$$

The last two terms, proportional to ψ and v^α, contribute to the first order in perturbations and the partial derivatives need to be computed, only to the zeroth order. The first term has two sources of perturbations from the partial derivatives: perturbations in the photon geodesic and the relation between the local and true coordinates. The former is nonzero, only when the derivative is taken with respect to $\tilde{z}$, i.e.,

$$\frac{1}{a} \epsilon_{\alpha\beta\gamma 0} \left(\frac{\partial x^\beta}{\partial \theta} \frac{\partial x^\gamma}{\partial \phi} \right)_0 \frac{\delta e^\alpha}{H(z)}, \tag{B7}$$

and the latter is

$$\frac{1}{a} \epsilon_{\alpha\beta\gamma 0} \left(\frac{\partial x^\alpha}{\partial z} \frac{\partial x^\beta}{\partial \theta} \frac{\partial x^\gamma}{\partial \phi} \right)_0 \left(\frac{\partial z}{\partial \tilde{z}} + \frac{\partial \theta}{\partial \tilde{\theta}} + \frac{\partial \phi}{\partial \tilde{\phi}} \right)_1, \tag{B8}$$

where the subscripts denote the order in perturbations, to which quantities in the bracket need to be computed. When combined together, Eq. (B6) is

$$\begin{aligned} u^d dS_d = &\frac{1}{a} \frac{\chi^2(z)}{H(z)} \sin\theta \times \left[1 + \delta e^\alpha e_\alpha + \left(\frac{\partial z}{\partial \tilde{z}} + \frac{\partial \theta}{\partial \tilde{\theta}} + \frac{\partial \phi}{\partial \tilde{\phi}} \right)_1 \right. \\ &\left. - \psi + v^\alpha e_\alpha \right]. \end{aligned} \tag{B9}$$

Finally, the determinant in Eq. (B1) gives $\sqrt{-g} = a^4(1 + \psi + 3\phi)$ and the total number of observed galaxies is

$$\begin{aligned} N_{\rm gal} = &\int a^3 n_{\rm phy} \frac{\chi^2(z)}{H(z)} \sin\theta d\tilde{z} d\tilde{\theta} d\tilde{\phi} \\ &\times \left[1 + 2\phi + \varepsilon + \left(\frac{\partial z}{\partial \tilde{z}} + \frac{\partial \theta}{\partial \tilde{\theta}} + \frac{\partial \phi}{\partial \tilde{\phi}} \right)_1 \right]. \end{aligned} \tag{B10}$$

From Eq. (B3), we obtain our final result,

$$\tilde{n} = n \frac{\chi^2(z)}{\chi^2(\tilde{z})} \frac{H(\tilde{z})}{H(z)} \left[1 + 2\phi - (1 + z) \frac{d\varepsilon}{dz} - 2\kappa \right], \tag{B11}$$

which includes the distortion of volume element δV and gravitational lensing magnification. This expression is manifestly gauge invariant and valid on all scales. In special relativity, the volume element of the local Lorentz frame of matter is distorted by $\gamma = \sqrt{1 - v^2}$, and hence is identical to an observer at rest, to the first order in perturbations. However, in our case the volume element can be measured, only by observing light rays of photons, of which time component is related to the spatial component, giving rise to the first order distortion in volume element.

[1] J. M. Bardeen, P. J. Steinhardt, and M. S. Turner, Phys. Rev. D **28**, 679 (1983).
[2] A. A. Starobinskij, Phys. Lett. **117B**, 175 (1982).
[3] S. W. Hawking, Phys. Lett. **115B**, 295 (1982).
[4] A. H. Guth and S.-Y. Pi, Phys. Rev. Lett. **49**, 1110 (1982).
[5] V. F. Mukhanov, H. A. Feldman, and R. H. Brandenberger, Phys. Rep. **215**, 203 (1992).
[6] A. G. Riess, A. V. Filippenko, P. Challis, A. Clocchiatti, A. Diercks, P. M. Garnavich, R. L. Gilliland, C. J. Hogan, S. Jha, R. P. Kirshner *et al.*, Astron. J. **116**, 1009 (1998).
[7] S. Perlmutter, G. Aldering, G. Goldhaber, R. A. Knop, P. Nugent, P. G. Castro, S. Deustua, S. Fabbro, A. Goobar, D. E. Groom *et al.*, Astrophys. J. **517**, 565 (1999).
[8] N. Kaiser, Astrophys. J. Lett. **284**, L9 (1984).
[9] D. J. Eisenstein, M. Blanton, I. Zehavi, N. Bahcall, J. Brinkmann, J. Loveday, A. Meiksin, and D. Schneider, Astrophys. J. **619**, 178 (2005).
[10] M. Tegmark *et al.*, Phys. Rev. D **74**, 123507 (2006).
[11] W. J. Percival, R. C. Nichol, D. J. Eisenstein, D. H. Weinberg, M. Fukugita, A. C. Pope, D. P. Schneider, A. S. Szalay, M. S. Vogeley, I. Zehavi *et al.*, Astrophys. J. **657**, 51 (2007).
[12] N. Padmanabhan *et al.*, Mon. Not. R. Astron. Soc. **378**, 852 (2007).
[13] Y. P. Jing, H. J. Mo, and G. Boerner, Astrophys. J. **494**, 1 (1998).
[14] U. Seljak, Mon. Not. R. Astron. Soc. **318**, 203 (2000).
[15] C.-P. Ma and J. N. Fry, Astrophys. J. **543**, 503 (2000).
[16] J. A. Peacock and R. E. Smith, Mon. Not. R. Astron. Soc. **318**, 1144 (2000).
[17] R. Scoccimarro, R. K. Sheth, L. Hui, and B. Jain, Astrophys. J. **546**, 20 (2001).
[18] A. A. Berlind and D. H. Weinberg, Astrophys. J. **575**, 587 (2002).
[19] A. Cooray and R. Sheth, Phys. Rep. **372**, 1 (2002).
[20] N. Kaiser, Mon. Not. R. Astron. Soc. **227**, 1 (1987).
[21] A. J. S. Hamilton, Astrophys. J. Lett.**385**, L5 (1992).
[22] T. Matsubara, Astrophys. J. **615**, 573 (2004).
[23] H.-J. Seo and D. J. Eisenstein, Astrophys. J. **665**, 14 (2007).
[24] T. Okumura, T. Matsubara, D. J. Eisenstein, I. Kayo, C. Hikage, A. S. Szalay, and D. P. Schneider, Astrophys. J. **676**, 889 (2008).
[25] E. Gaztanaga, A. Cabre, and L. Hui, arXiv:0807.3551.
[26] U. Seljak, Astrophys. J. **463**, 1 (1996).
[27] R. Narayan, Astrophys. J. Lett. **339**, L53 (1989).
[28] R. Scranton *et al.*, Astrophys. J. **633**, 589 (2005).
[29] C. Blake, A. Pope, D. Scott, and B. Mobasher, Mon. Not. R. Astron. Soc. **368**, 732 (2006).
[30] T. Matsubara, Astrophys. J. Lett. **537**, L77 (2000).
[31] A. Vallinotto, S. Dodelson, C. Schimd, and J.-P. Uzan, Phys. Rev. D **75**, 103509 (2007).
[32] L. Hui, E. Gaztanaga, and M. LoVerde, Phys. Rev. D **76**, 103502 (2007).
[33] M. Tegmark *et al.*, Phys. Rev. D **74**, 123507 (2006).
[34] D. N. Spergel *et al.*, Astrophys. J. Suppl. Ser. **170**, 377 (2007).
[35] E. Komatsu, J. Dunkley, M. R. Nolta, C. L. Bennett, B. Gold, G. Hinshaw, N. Jarosik, D. Larson, M. Limon, L. Page *et al.*, arXiv:0803.0547.
[36] J. M. Bardeen, Phys. Rev. D **22**, 1882 (1980).
[37] H. Kodama and M. Sasaki, Prog. Theor. Phys. Suppl. **78**, 1 (1984).
[38] J.-C. Hwang and H. Noh, Phys. Rev. D **65**, 023512 (2001).
[39] W. Hu, arXiv:astro-ph/0402060.
[40] R. K. Sachs and A. M. Wolfe, Astrophys. J. **147**, 73 (1967).
[41] J.-C. Hwang and H. Noh, Phys. Rev. D **59**, 067302 (1999).
[42] B. Jain, U. Seljak, and S. White, Astrophys. J. **530**, 547 (2000).
[43] C. M. Hirata and U. Seljak, Phys. Rev. D **67**, 043001 (2003).
[44] R. Blandford and R. Narayan, Astrophys. J. **310**, 568 (1986).
[45] I. I. Shapiro, Phys. Rev. Lett. **13**, 789 (1964).
[46] M. A. Strauss and J. A. Willick, Phys. Rep. **261**, 271 (1995).
[47] A. J. S. Hamilton, in *The Evolving Universe*, edited by D. Hamilton, Astrophysics and Space Science Library Vol. 231 (Kluwer Academic Publishers, Dordrecht, The Netherlands, 1998), p. 185.
[48] W. Hu and A. Cooray, Phys. Rev. D **63**, 023504 (2000).
[49] M. Bartelmann, Astron. Astrophys. **298**, 661 (1995).
[50] B. Jain, Astrophys. J. Lett. **580**, L3 (2002).
[51] B. Jain, R. Scranton, and R. K. Sheth, Mon. Not. R. Astron. Soc. **345**, 62 (2003).
[52] R. Moessner and B. Jain, Mon. Not. R. Astron. Soc. **294**, L18 (1998).
[53] R. E. Smith, J. A. Peacock, A. Jenkins, S. D. M. White, C. S. Frenk, F. R. Pearce, P. A. Thomas, G. Efstathiou, and H. M. P. Couchman, Mon. Not. R. Astron. Soc. **341**, 1311 (2003).
[54] D. N. Limber, Astrophys. J. **119**, 655 (1954).
[55] L. Hui, E. Gaztañaga, and M. Loverde, Phys. Rev. D **77**, 063526 (2008).
[56] S. Cole, K. B. Fisher, and D. H. Weinberg, Mon. Not. R. Astron. Soc. **267**, 785 (1994).
[57] D. H. Weinberg, T. Beers, M. Blanton, D. Eisenstein, H. Ford, J. Ge, B. Gillespie, J. Gunn, M. Klaene, G. Knapp *et al.*, in *American Astronomical Society Meeting Abstracts* (Institute of Physics (IOP), Philadelphia, PA, 2007), Vol. 211, p. 132.10.
[58] D. J. Schlegel, M. Blanton, D. Eisenstein, B. Gillespie, J. Gunn, P. Harding, P. McDonald, R. Nichol, N. Padmanabhan, W. Percival *et al.*, in *American Astronomical Society Meeting Abstracts* (Institute of Physics (IOP), Philadelphia, PA, 2007), Vol. 211, p. 132.29.
[59] U. Seljak and M. Zaldarriaga, Astrophys. J. **469**, 437 (1996).
[60] I. Zehavi *et al.*, Astrophys. J. **630**, 1 (2005).
[61] J. Yoo, J. L. Tinker, D. H. Weinberg, Z. Zheng, N. Katz, and R. Davé, Astrophys. J. **652**, 26 (2006).
[62] P. J. E. Peebles and J. T. Yu, Astrophys. J. **162**, 815 (1970).
[63] R. A. Sunyaev and Y. B. Zeldovich, Astrophys. Space Sci. **7**, 3 (1970).
[64] C. Blake, A. Collister, S. Bridle, and O. Lahav, Mon. Not. R. Astron. Soc. **374**, 1527 (2007).
[65] D. J. Eisenstein, I. Zehavi, D. W. Hogg, R. Scoccimarro, M. R. Blanton, R. C. Nichol, R. Scranton, H.-J. Seo, M. Tegmark, Z. Zheng *et al.*, Astrophys. J. **633**, 560 (2005).

[66] N. P. Ross, T. Shanks, R. D. Cannon, D. A. Wake, R. G. Sharp, S. M. Croom, and J. A. Peacock, Mon. Not. R. Astron. Soc. **387**, 1323 (2008).
[67] W. E. Ballinger, J. A. Peacock, and A. F. Heavens, Mon. Not. R. Astron. Soc. **282**, 877 (1996).
[68] R. Scoccimarro, Phys. Rev. D **70**, 083007 (2004).
[69] U. Seljak, Mon. Not. R. Astron. Soc. **325**, 1359 (2001).
[70] M. White, Mon. Not. R. Astron. Soc. **321**, 1 (2001).
[71] J. L. Tinker, Mon. Not. R. Astron. Soc. **374**, 477 (2007).
[72] J. Guzik, G. Bernstein, and R. E. Smith, Mon. Not. R. Astron. Soc. **375**, 1329 (2007).
[73] D. J. Eisenstein, J. Annis, J. E. Gunn, A. S. Szalay, A. J. Connolly, R. C. Nichol, N. A. Bahcall, M. Bernardi, S. Burles, F. J. Castander *et al.*, Astron. J. **122**, 2267 (2001).
[74] I. Zehavi *et al.*, Astrophys. J. **621**, 22 (2005).
[75] D. Eisenstein and M. White, Phys. Rev. D **70**, 103523 (2004).
[76] H.-J. Seo and D. J. Eisenstein, Astrophys. J. **633**, 575 (2005).
[77] D. J. Eisenstein, H.-J. Seo, and M. White, Astrophys. J. **664**, 660 (2007).
[78] M. Crocce and R. Scoccimarro, Phys. Rev. D **77**, 023533 (2008).
[79] M. Loverde, L. Hui, and E. Gaztañaga, Phys. Rev. D **77**, 023512 (2008).
[80] C. Alcock and B. Paczyński, Nature (London) **281**, 358 (1979).
[81] J. Yoo, D. H. Weinberg, J. L. Tinker, Z. Zheng, and M. S. Warren, arXiv:0808.2988.
[82] N. Kaiser, Astrophys. J. **388**, 272 (1992).
[83] P. Simon, Astron. Astrophys. **473**, 711 (2007).
[84] M. LoVerde and N. Afshordi, Phys. Rev. D **78**, 123506 (2008).
[85] S. Weinberg, *Gravitation and Cosmology: Principles and Applications of the General Theory of Relativity*, edited by Steven Weinberg (Wiley-VCH, New York, 1972), ISBN 0-471-92567-5, p. 688.
[86] L. Jiang *et al.*, Astron. J. **131**, 2788 (2006).